Soil Dynamics and Earthquake Engineering 181 (2024) 108633

Contents lists available at ScienceDirect

Soil Dynamics and Earthquake Engineering

journal homepage: www.elsevier.com/locate/soildyn

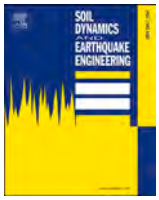

Soil amplification in the Santiago city, Chile, due to shallow crustal earthquakes

Fabián Ortiz [a], César Pastén [b,*], José Bustos [b], Sergio Ruiz [c], Rodrigo Astroza [d], Gabriel Easton [e]

[a] IDIEM, University of Chile, Chile
[b] Department of Civil Engineering, University of Chile, Av. Blanco Encalada 2002, Of. 431, Santiago, 8370449, Chile
[c] Department of Geophysics, University of Chile, Chile
[d] Facultad de Ingeniería y Ciencias Aplicadas, Universidad de Los Andes, Chile
[e] Department of Geology, University of Chile, Chile

ARTICLE INFO

Keywords:
Physics-based numerical simulations
Site effects
Seismic amplification
Shear-wave velocity model
Ground motion models

ABSTRACT

Three-dimensional physics-based numerical simulations (3D-PBS) of the seismic response of the Santiago Basin, Chile, were performed considering a large-scale velocity model and shallow crustal earthquake scenarios, associated with the west-verging thrust San Ramón Fault. Numerical results show that competent gravelly soils in the center of the basin respond with low seismic amplification and shorter durations of strong ground motions, unlike less competent fine-grained soils in the northern area. A significant increase in the seismic intensities is observed in the vicinity of rock outcrops, attributable to the generation of surface waves. Seismic amplification factors were calculated with respect to a reference site on gravel and their values show high levels of amplification in the vicinity of the seismic source, and on soils with low shear wave velocities (V_s) and long fundamental vibration periods. On the other hand, empirical ground motion models (GMM) were used to estimate amplification factors for peak ground accelerations and spectral accelerations at various periods. Results from GMMs and 3D-PBS were compared, showing similarities in the attenuation pattern on stiff soils, but differences in soils with low V_s. Moreover, 3D-PBS captured site effects associated with the local geomorphology, unlike GMMs.

1. Introduction

The Santiago Basin, located in Central Chile (Fig. 1), is home to more than 7 million inhabitants, about 40 % of the total population of the country [1], in a seismically active region, controlled by the subduction of the Nazca Plate underneath the South American Plate. Some of the most recent earthquakes in the region are the 1985 Mw 8.0 Valparaíso and the 2010 Mw 8.8 Maule megathrust earthquakes, as well as the 1958 Ms 7.0 Las Melosas shallow crustal earthquake [2]. Due to the socioeconomic importance of Santiago city, the study of its seismic response has gained special interest.

Previous studies have shown that ground motion amplifications and variations in the motion frequency content are caused by the variability in the soil's dynamic properties and topographic irregularities in different zones of the basin. Acevedo [3] developed an updated 3D velocity model for the Santiago Basin, based on results from surface wave methods, seismic noise interferometry, the RayDec method, and the horizontal-to-vertical spectral ratio (HVSR) method, which were used to perform a three-dimensional physics-based numerical simulation (3D-PBS). The 3D model was subjected to two seismic scenarios and found that the Santiago Gravels (Soil unit II in Fig. 1) respond with low seismic amplification due to their high shear wave velocities (V_s), a smooth V_s increase with depth, and low impedance contrast with the underlying bedrock. In contrast, the fine-grained soils in the northwestern part of the city (Soil unit VII in Fig. 1) show higher amplification due to their lower V_s, variability in bedrock depth, and lateral variations of V_s. In addition, the numerical simulations predict relative amplifications in fine-grained soils that are similar to those obtained from real seismic events ($5.0 < Mw < 6.7$). Subsequently, Bustos et al. [4] modeled the seismic response of three large-scale 2D cross-sections of the basin, showing that its geometry and difference in soil types modifies the surface response, with longer ground motion durations in the northern, northwestern, and western zones of the basin (Soil units VI and VII in Fig. 1), and with rapid ground motion attenuation in the

* Corresponding author.
E-mail addresses: Fabian.ortiz@ug.uchile.cl (F. Ortiz), cpasten@uchile.cl (C. Pastén), jose.bustos.f@ug.uchile.cl (J. Bustos), sruiz@uchile.cl (S. Ruiz), rastroza@miuandes.cl (R. Astroza), geaston@uchile.cl (G. Easton).

https://doi.org/10.1016/j.soildyn.2024.108633
Received 29 December 2023; Received in revised form 22 March 2024; Accepted 1 April 2024

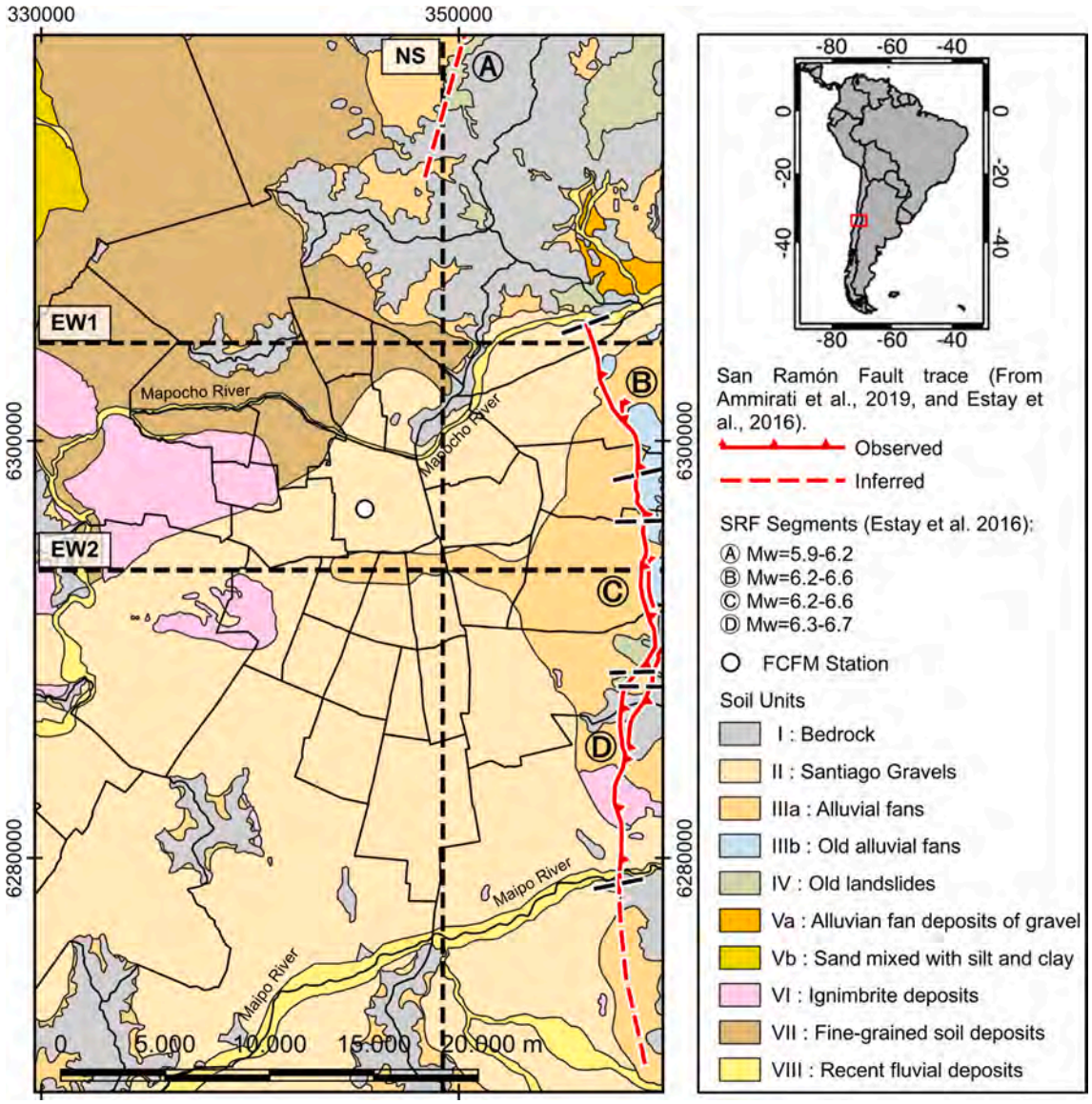

Fig. 1. Surface geology of the Santiago Basin based on Leyton et al. [27]. The San Ramón Fault trace is shown as a red line, divided into four segments according to Estay et al. [11]. The scarp is extended to the south (below segment D) as proposed by Ammirati et al. [6]. The three cross-sections analyzed in this study (EW1, EW2, and NS) are shown in black segmented lines.

central, southern, and eastern zones dominated by the Santiago Gravels. Aggravation factors for two-dimensional versus one-dimensional simulations showed that the 1D approach provides similar results to 2D simulations in areas with stiff soils but fails to capture surface waves generated in soft soils at the edges of rock outcrops, which is captured by the 2D approach. This result underscores that 1D simulations are unable to adequately represent the phenomena observed during seismic events, a conclusion also drawn by other studies, such as Ozaslan et al. [5] in the Gemlik Basin, Turkey.

It is worth mentioning that both studies conducted on the Santiago Basin described above considered plane wavefronts as seismic input, which can be associated with deep or very distant earthquakes. It is not evident that the seismic response found in these studies would prevail if the basin was subjected to shallow crustal earthquakes, such as those that could be triggered by the San Ramón Fault (SRF, Fig. 1).

The SRF is a reverse fault system located east of the Santiago City, on the border with the western flank of the Andes Mountains, with an extension of about 40–50 km in the north-south direction. Studies have shown that this system can be considered active, with associated seismicity between 10 and 25 km depth, average displacements between 0.1 and 0.5 mm/year, and a recharge period close to 9000 years [6–10]. According to Estay et al. [11], the SRF could be discontinuous, with several segments (segments A to D in Fig. 1) capable of triggering earthquakes with magnitudes up to Mw 6.7. On the other hand, Vargas et al. [10] reported that the largest possible earthquake that could be triggered by the SRF would be a magnitude Mw 7.5, corresponding to the rupture of the entire fault plane.

Earthquakes associated with shallow crustal faults can cause large socio-economic impacts, such as the 1994 Mw 6.7 Northridge Earthquake, which caused nearly 60 deaths, financial losses estimated at 13 to 20 billion dollars (the most costly earthquake in U.S. history to date), as well as destruction and severe damage to buildings [12]. Another example is the 1999 Chichi Mw 7.6 earthquake, which ruptured an approximately 100 km segment of the Chelungpu thrust fault, resulting in more than 2400 people dead and more than 11,000 injured [13], more than 8500 buildings destroyed, and economic losses estimated to be close to 10–12 billion dollars [14]. Given the devastating consequences of shallow crustal earthquakes, there is concern about the potential seismic risk associated with the activation of the SRF in the city of Santiago. Thus, several studies based on the application of PBSs and

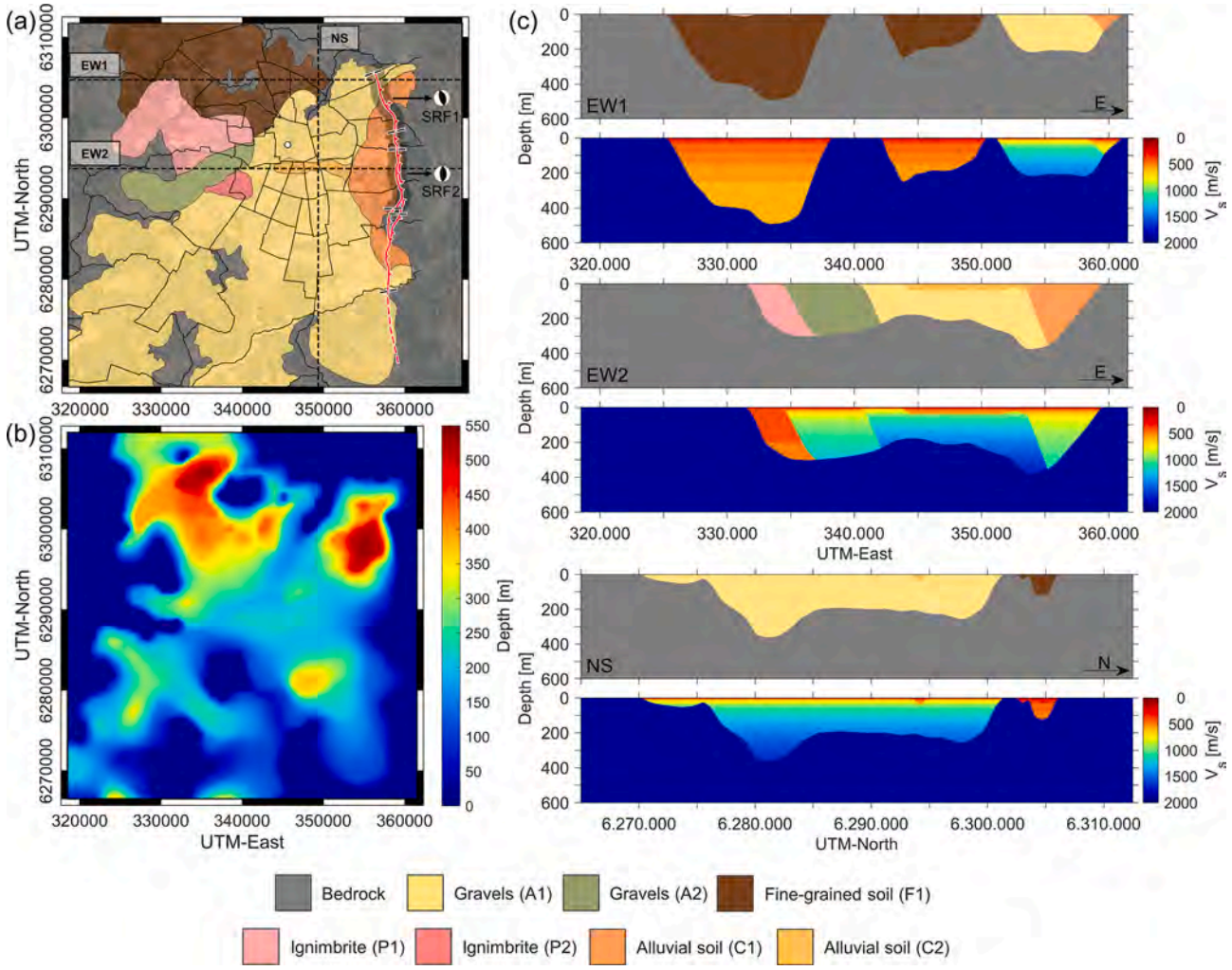

Fig. 2. (a) Plan view of the 3D sedimentary model considered for the Santiago Basin with the three cross-sections analyzed in this study and the SRF trace. The shaded areas on the trace show the segments considered in the SRF1 and SRF2 simulations. The focal mechanism of each case is shown to the right of each segment, in the location of each epicenter. (b) Depth distribution of the sedimentary model. (c) Cross-sections EW1, EW2, and NS. Shear wave velocities are shown below each cross-section.

ground motion models (GMMs) have been evaluated to obtain the seismic response of the Santiago Basin to earthquakes associated with the SRF.

In this context, PBSs have emerged as a robust method for conducting small- and large-scale seismic risk analyses. These numerical simulations provide synthetic ground motion time histories reflecting the physics of the seismic wave propagation problem from the source up to the site of interest, including directivity effects in the near-field, as well as topographic and complex site effects [15], thus allowing prediction of ground motion variability [16]. Cortés [17] performed PBSs for the SRF activation, considering a model of the Santiago Basin with a uniform soil layer on top of the bedrock, and a 40 km long and 20 km wide fault surface. The simulations were performed for 8 seismic scenarios with moment magnitudes Mw ranging from 6.0 to 7.0 and considered linear visco-elastic (LE) and non-linear elastic (NLE) soil models. The results of the PBSs at the model surface were peak ground velocities (PGV), peak ground accelerations (PGA), and spectral accelerations at various periods (Sa(T)). In addition, the study evaluated the GMM developed by Cauzzi et al. [18] to estimate PGAs and PGVs. The results show that PBSs can capture site effects due to the topography of the area and soil properties, unlike the results from GMM. Despite the differences, this study highlights that both methods predict relatively similar average peak ground motion distribution and attenuation patterns from the seismic source. On the other hand, Ammirati et al. [6] proposed a seismic scenario for a magnitude Mw 7.5 earthquake evaluated with two GMMs [19,20] that considered a 50 km long and 20 km wide fault plane. The results show PGAs close to 0.7–0.9 g in the vicinity of the fault scarp, values that are consistent with Cortés's [17] results in the same zone, while being much larger than the PGAs recorded during the 2010 Mw 8.8 Maule megathrust earthquake in the central-eastern area of Santiago (PGA ≈ 0.3g in Soil unit III, Fig. 1) and the ignimbrite deposits (PGA = 0.56g in Soil unit VI, Fig. 1), according to Boroschek et al. [21].

The objectives of this study are (1) to implement a 3D-PBS of the Santiago Basin, using the updated velocity model developed by Acevedo [3] with different soil units, (2) to simulate two seismic events associated with the activation of two segments of the SRF (segments B and C in Fig. 1), (3) to study the seismic behavior of the basin in terms of ground motion duration, PGA, Sa, predominant vibration periods, among others, (4) to implement three GMMs [18–20] for the estimation of the relative seismic demand and (5) to compare the surface response of both methodologies and judge their applicability in ground motion estimations.

Table 1
Dynamic properties of the soil units [3].

Soil Unit	Depth z (m)	V_s (m/s)	V_{s30} (m/s)	V_p (m/s)	Poisson Ratio ν (−)	Density (kg/m^3)
A1	0–10	400	579	748	0.3	2100
	10–20	700		1310		
	20–30	800		1497		
	30–530	$V_S(z) = 800 + 49.2\sqrt{z-30}$		$V_P(z) = 1497 + 92.0\sqrt{z-30}$		
A2	0–10	300	437	561	0.3	2000
	10–20	500		935		
	20–30	650		1216		
	30–350	$V_S(z) = 650 + 36.3\sqrt{z-30}$		$V_P(z) = 1216 + 67.9\sqrt{z-30}$		
F1	0–10	200	290	356	0.27	1800
	10–30	350		624		
	30–80	450		802		
	80–150	500		891		
	150–250	550		980		
	250–450	600		1069		
P1	0–10	350	382	624	0.27	1700
	10–200	400		713		
	200–600	500		891		
P2	0–10	350	469	624	0.27	1700
	10–20	500		891		
	20–40	650		1158		
	40–600	$V_S(z) = 800 + 49.2\sqrt{z-30}$		$V_P(z) = 1497 + 92.0\sqrt{z-30}$		
C1	0–10	300	415	561	0.3	2000
	10–20	450		842		
	20–30	600		1123		
	30–450	$V_S(z) = 600 + 29.3\sqrt{z-30}$		$V_P(z) = 1123 + 54.8\sqrt{z-30}$		
C2	0–10	300	407	561	0.3	2000
	10–20	450		842		
	20–50	550		1029		
	50–600	$V_S(z) = 800 + 49.2\sqrt{z-30}$		$V_P(z) = 1497 + 92.0\sqrt{z-30}$		

Table 2
Dynamic properties of bedrock.

Depth [m]	V_s (m/s)	V_p (m/s)	Poisson Ratio ν (−)	Density (kg/m^3)
0–600	1900	3555	0.3	2600
600–1000	2300	4303		
1000–2000	2500	4677		
2000–2500	3000	5612		
>2500	3600	6735		

2. Geological framework

The Santiago Basin is a topographic depression filled with quaternary sediments [22] that has an approximate extension of 40 km in the east-west direction and 90 km in the north-south direction, with very gentle slopes and elevations ranging from 450 to 700 m above sea level [23]. Gravimetric studies show that the underlying bedrock morphology is irregular, with depocenters that can reach 500 m depth [24–26].

The soil units in the basin (Fig. 1) are described in Leyton et al. [27], which is an update of the surface geology map elaborated by Valenzuela [28]. In the central and southern parts of the basin, there are mainly deposits of sub-angular blocks and gravels in a sand-clay matrix, with intercalations of sand, silt, and clay, originated by the materials transported by the Mapocho and Maipo rivers. These soils, called Santiago Gravels (Soil unit II in Fig. 1), have high strength, stiffness, and shear wave velocities. To the east of the basin, alluvial fans were formed by gravitational action at the foot of the Andes Mountains (Soil units IIIa, IIIb, and Va in Fig. 1), composed mainly of blocks and gravels with intercalations of sands, silts, and clays. These soils are moderately stiff. To the west of the basin, volcanic ashes, called Pudahuel Ignimbrite (unit VI in Fig. 1), can be found in terraces thicker than 20 m with intercalations of gravel, sand, and silt. To the north and northwest of the basin, silt and clay deposits are found with some intercalated gravels (unit VII in Fig. 1). Units VI and VII correspond mainly to soft soils with low stiffness and strength.

3. Numerical model

The large-scale three-dimensional model developed to study the seismic response of the Santiago Basin subjected to the activation of the SRF, considering the different soils' dynamic properties, the finite-difference code, and the two seismic scenarios, is detailed below.

3.1. Three-dimensional geological-sedimentary model

The sedimentary model of the basin considered in this work (Fig. 2) is based on the updated model proposed by Acevedo [3], which extends and simplifies the surface geology presented by Leyton et al. [27]. This updated model defines the bedrock depth and 7 soil units based on the results of the HVSR method in each unit and shear wave velocity profiles (V_s) obtained with surface wave methods. The units are gravels (units A1 and A2), fine-grained soil (unit F1), ignimbrite (units P1 and P2), and alluvial soils (units C1 and C2). According to Acevedo [3], the depth of the bedrock underlying the soil was obtained from gravimetric studies [24,25], except in units F1 and P1 where the depth was estimated by adjusting the peak of a measured HVSR curve to the peak of the theoretical Rayleigh wave ellipticity at the locations, calculated from the V_s profiles of the soil units.

3.2. Dynamic properties

In the new velocity model proposed by Acevedo [3], each soil unit was assigned a characteristic V_s profile, obtained by inverting all available phase velocity dispersion curves in a soil unit and assuming that the HVSR is the Rayleigh wave ellipticity [3]. The V_s profiles were defined as a stack of 10 m thick layers. Moreover, the V_s of the 3 shallowest layers were assigned such that the resulting averaged shear-wave velocity of the upper 30 m (V_{s30}) matched the values measured in situ. The functions defining V_s profiles of the soil units are shown in Table 1.

Compressional wave velocities (V_p) were obtained considering the Poisson's ratio ν and the theory of elasticity with Equation (1). The densities, also shown in Table 1, were adopted from Bonnefoy-Claudet et al. [29].

$$V_p = V_s\sqrt{\frac{2(1-\nu)}{1-2\nu}} \tag{1}$$

V_s of the bedrock was adjusted to the results in Salomón et al. [30], considering a total of 5 layers with V_s values ranging from 1900 m/s in the top layer to 3600 m/s for depths larger than 2.5 km (Table 2).

Quality factors were defined for S- and P-waves, according to Equations (2) and (3) [31], which are inversely proportional to damping ξ ($2Q = 1/\xi$).

$$Q_S = \frac{V_S}{10} \tag{2}$$

$$Q_P = 2{\cdot}Q_s \tag{3}$$

The maximum damping levels in the model are found near the surface, where Q_S and Q_P reach their minima. Considering the V_s values of each soil unit near the surface (Table 1), the largest damping values are close to $\xi \approx 2.5$ % in unit F1, $\xi \approx 1.7$ % in units A2, C1, and C2, $\xi \approx 1.4$ %

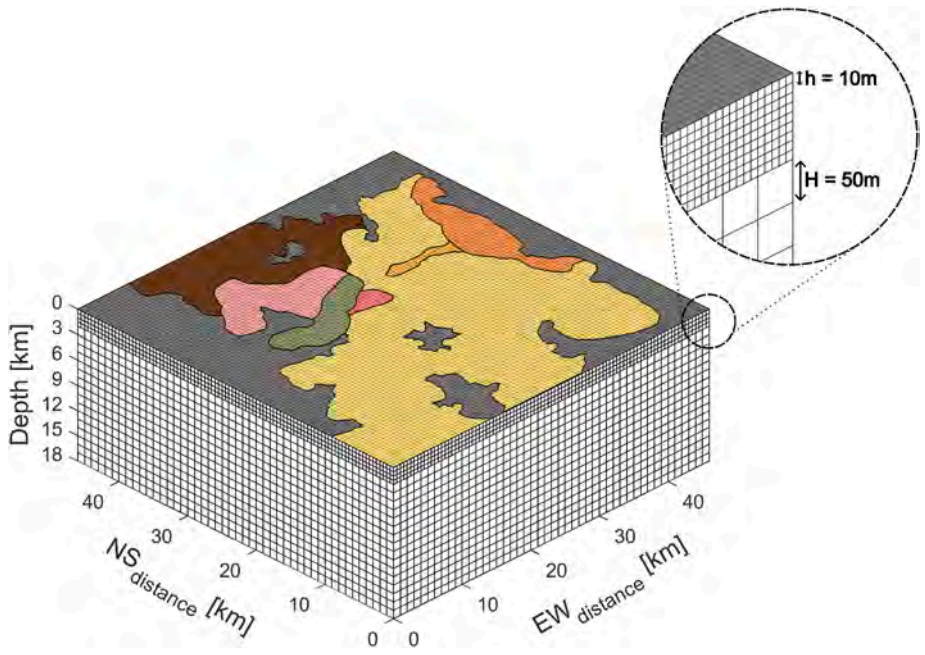

Fig. 3. Sketch of the 3D model and the finite difference grid, with the different soil units. Note that the dimensions of the grid elements are not to scale with the values of the axes.

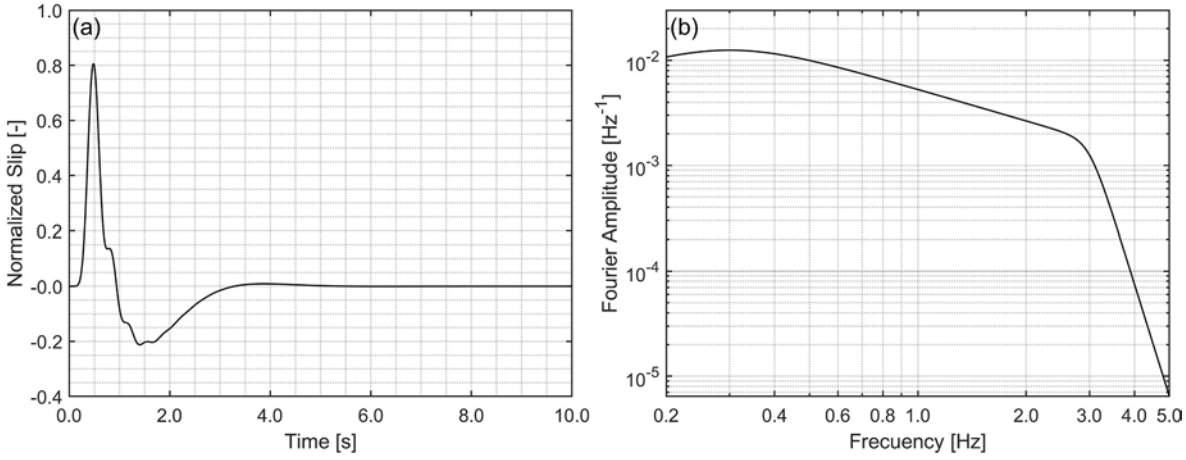

Fig. 4. Source function used in the simulations. (a) Normalized displacement in time and (b) Fourier amplitude of the source function.

Table 3
Hypocentral location and focal mechanism of the simulated events.

Event	East coordinate (UTM)	North coordinate (UTM)	Strike (°)	Dip (°)	Rake (°)	Depth (km)
FSR 1	363,850	6,302,472	343	34	90	15
FSR 2	363,850	6,293,204	0	34	90	15

in units P1 and P2, and $\xi \approx 1.25$ % in unit A1. These values decay rapidly with depth as V_s increases.

3.3. Physics-based numerical simulations

Numerical simulations were performed using the finite-difference (FD) code FDSim3D, which allows the propagation of seismic waves generated by an earthquake in three-dimensional media, with a flat free surface [32]. The adopted viscoelastic constitutive model is a Generalized Maxwell body (GMB-EK, defined by Ref. [33]). The computational algorithm is based on an explicit FD scheme that solves equations of motion for a heterogeneous viscoelastic medium with material interfaces [34]. In this regard, the code uses a (2, 4) velocity-stress (VS) scheme, 2nd-order accurate in time and 4th-order accurate in space, which is constructed on a staggered FD grid.

For the computational region of the model, FDSim3D generates a discrete parallelepiped from the intersection of representative volumes of each soil unit, on which a discontinuous grid is defined. Each grid point adopts the dynamic properties of the soil unit or the bedrock where it is located. In addition, the code allows dividing the model into an upper section (where the soil units under study are located) with a finer spatial discretization compared to the lower section (bedrock only), which optimizes computational resources and execution time. A graphical representation of the model is shown in Fig. 3.

Boundary conditions are defined using Perfectly Matched Layers (PML), validated by Kristek et al. [35], which prevent seismic wave reflection at the edges of the model. To ensure numerical stability, the time step Δt, defined as a function of the maximum wave velocity V_p^* and

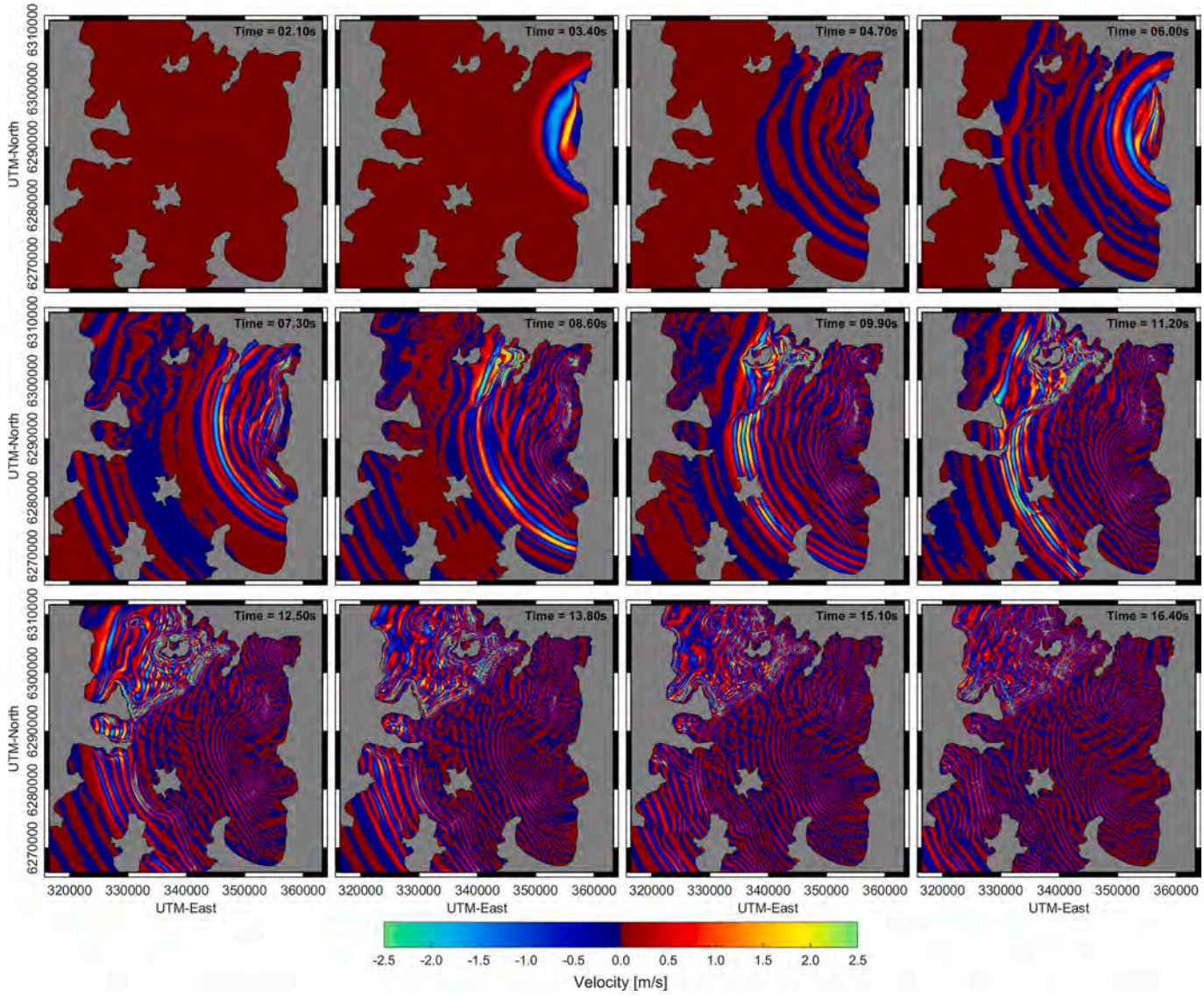

Fig. 5. Snapshots of vertical ground motions from SRF2 simulation (Time step = 1.3 s).

the corresponding grid spacing h, must satisfy the stability condition for the (2, 4) staggered-grid VS FD scheme used in the code as follows [32]

$$\Delta t \leq \frac{6}{7\sqrt{3}} \cdot \frac{h}{V_p^*} \tag{4}$$

The maximum credible frequency f_{max} of the simulation can be estimated from the minimum velocity $V_{S\,min}$ and the associated grid spacing h [36]

$$f_{max} \approx \frac{V_{Smin}}{6h} \tag{5}$$

The model is 46 km in the north-south direction, 46 km in the east-west direction, and 18 km in depth, with a fine grid spacing h = 10 m from the free surface to 2 km depth, and a coarse grid spacing H = 50 m from 2 km depth to the base of the model, as seen in Fig. 3. Considering $V_p^* = 4677$ m/s, the maximum Vp from the surface up to 2 km depth, and the minimum spacing h = 10 m, a time step Δ t = 0.001s is obtained with Equation (4). For larger depths, V_p exceeds 5500 m/s (Table 2), allowing larger grid spacings (H = 50 m) for the same time step. The adopted grid spacings ensure the numerical stability of the model. On the other hand, the minimum value of V_s in the model is close to 200 m/s near the surface in soil unit F1, which results in a maximum credible frequency of 3.3 Hz for this unit, according to Equation (5). The maximum credible frequency increases to ≥ 5 Hz for the other soil units with minimum V_s close to 300 m/s.

Regarding the seismic source, there are mainly two alternatives to simulate the waves propagating from an earthquake source, either from the full extent of a fault or from a point-source approximation. As described by Xu & Knopoff [37], the first case requires accounting for geometric complexities along a fault to fully account for the variable ground motions observed in real earthquakes, hence, inhomogeneity is a critical property of earthquake models. This is also detailed in Bizzarri [38], who points out that all geometrical complexities of the source, spatial heterogeneities, details of the stress release, and the forces acting on the failure interface must be considered, which is rather challenging to achieve. On the other hand, the point-source approximation considers that all of the energy released by an earthquake is concentrated in one or more double couple (DC) points, which are pairs of couples whose torques cancel each other [39], accounting for the average fault geometry and the seismic moment of the earthquake.

FDSim3D allows two options to simulate earthquakes, either to use vertical and horizontal plane wavefronts coming from the base of the model, or to implement DC points inside the model domain. In both cases, a source function that defines the body waves generated at the

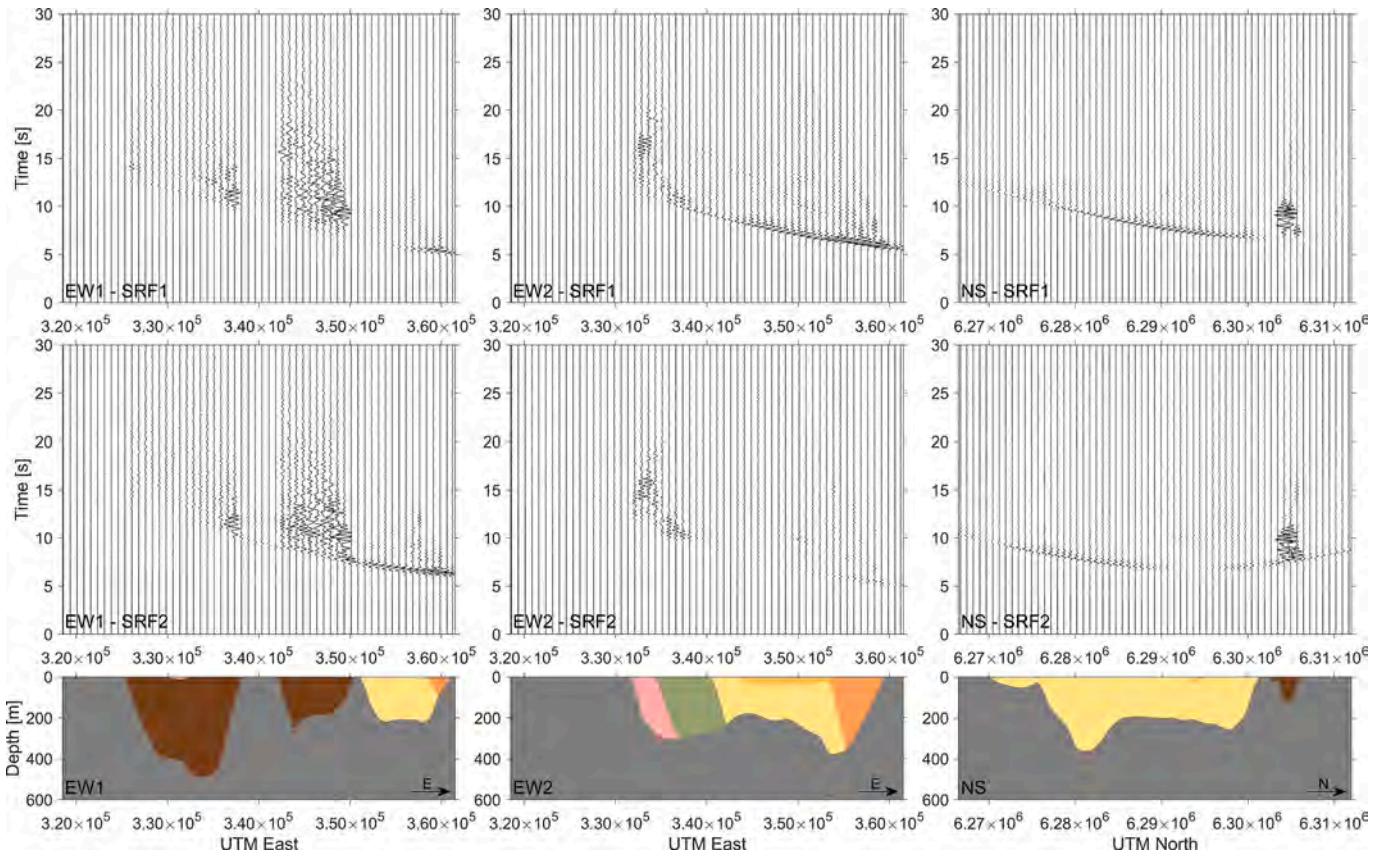

Fig. 6. Velocity ground motions in the EW direction along cross-sections EW1, EW2, and NS, for simulations of SRF1 (upper panels) and SRF2 (middle panels). The bedrock depth and the different soil units are shown in the lower panels. The legend is the same as that in Fig. 2.

seismic source is required. While plane wavefronts can be associated with deep or very distant earthquakes, which is not representative of shallow crustal earthquakes addressed herein, the second option allows us to freely locate DC points on the SRF plane; therefore, we decided to use this option in our simulations.

The code requires a normalized-displacement time function as the input of the seismic source (Fig. 4). This study adopts one used by Moczo et al. [32] and is described as $s(t) = K{\cdot}D(t)$, with K a constant and $D(t)$ a bandpass filtered Dirac delta function. The amplitude of the source function decays at about 3–5 Hz, consistent with the maximum credible frequency obtained for the adopted soil velocity model and grid spacing.

3.4. Seismic scenarios

Two seismic scenarios associated with the activation of the SRF, named SRF1 and SRF2, were simulated. These scenarios are directly related to the activation of segments B and C shown in Fig. 1, which were defined based on the surface manifestation of the SRF and supported by results of gravity profiles and the fluctuation of the sinuosity index along the fault trace [11]. These two segments were selected since they are closer to the most populated areas and critical infrastructure, as well as to the northern and northwestern fine-grained soils, which are of particular interest due to their poor dynamic properties.

For the two selected segments, Estay et al. [11] obtained the scalar seismic moment (M_0) using the equation defined in Aki & Richards [40], and the moment magnitude (Mw) using the equation defined in Hank & Kanamori [41], considering an approximate shear modulus $\mu = 3 \times 10^{10}$ Nm^{-2}, a fault width in the 10–15 km range, and an average slip of 4 m, thus obtaining moment magnitudes in the range of Mw 6.2 to 6.7.

A proper simulation of large magnitude earthquakes (e.g. the maximum credible earthquake Mw 7.5, [10]) using DC points requires defining the initial rupture location and the spatial distribution of a series of DC points on the fault plane, which can be sequentially triggered to represent the propagation direction and the rupture velocity. Unfortunately, this detailed information is unavailable since studies that characterize the rupture process of the SRF have not been performed. A valid option in the absence of this information would be to assume different combinations of rupture initiation locations, propagation directions, and rupture velocities for the fault plane and perform several numerical simulations, which is beyond the scope of this work due to our limited computational capacity.

Considering the next best feasible approximation, two selected seismic scenarios were modeled with singular DC points in the middle of each fault segment, striking according to the approximate fault traces in Fig. 2a (343° and 0° for SRF1 and SRF2 simulations, respectively). The study of Ammirati et al. [6] was considered to define the direction and depth of the DC points, in which an east-dipping fault plane of ~34° was estimated, with associated seismicity between 10 and 25 km depth. DC points were located at a depth of 15 km. Finally, a magnitude Mw. 6.0 was considered for the two seismic scenarios, which is slightly lower than the maximum magnitudes estimated by Estay et al. [11] for the segments B and C of the SRF. This decision allows for the adoption of the DC point approach to be valid. A summary of the characteristics of the simulated seismic events (SRF1 and SRF2) is presented in Table 3 whereas their epicenters and focal mechanisms are shown in Fig. 2a.

4. 3D-PBS results

Fig. 5 shows snapshots of vertical ground motions resulting from SRF2 simulation. Arrivals of p-waves at the model surface at t = 3.4 s (frame 2) are followed by s-waves at t = 6.0 s (frame 4). Waves travel to the west of the basin up to t = 15 s, approximately, after which surface

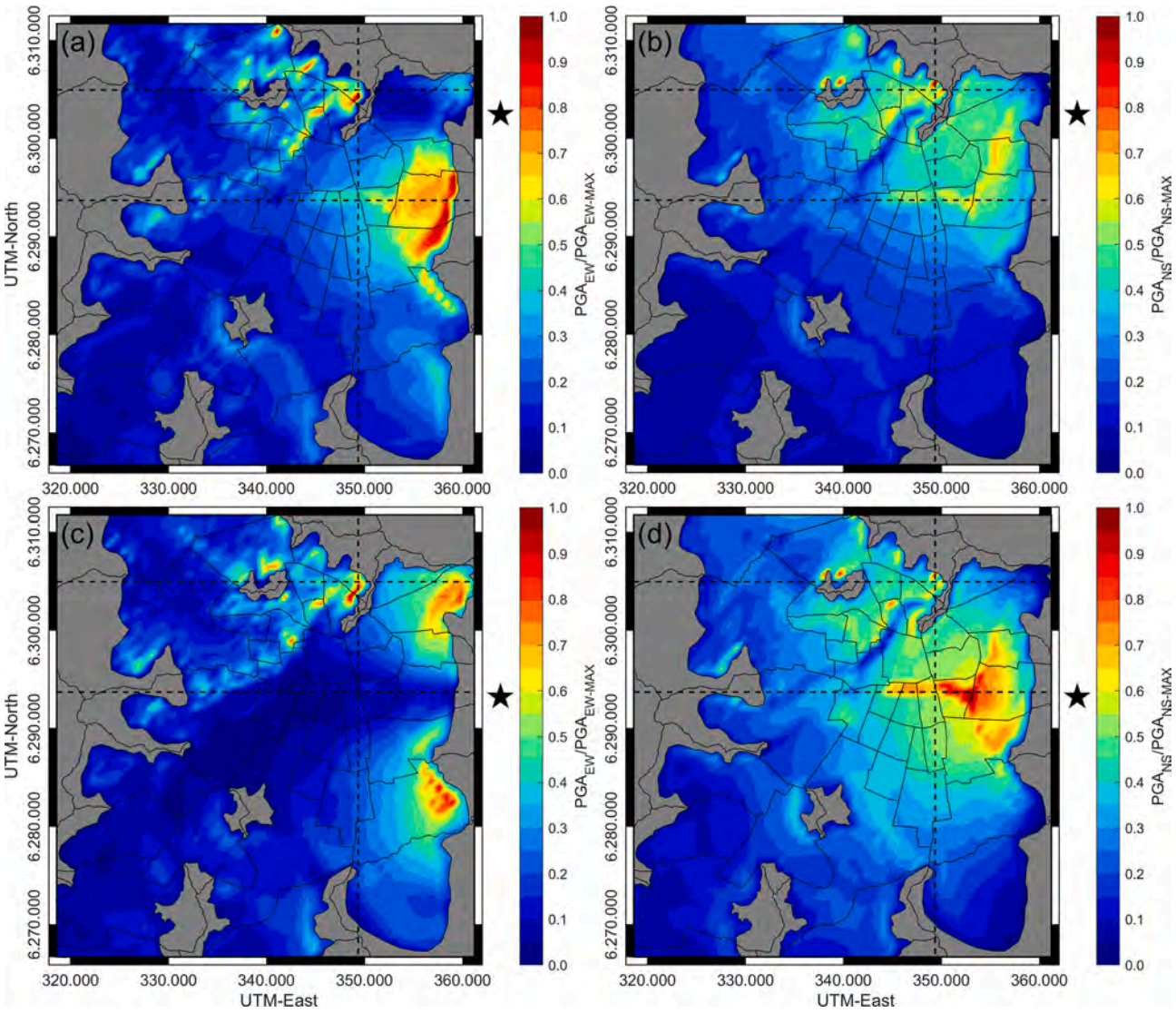

Fig. 7. PGA in the EW direction for (a) SRF1 and (c) SRF2, and in the NS direction for (b) SRF1 and (d) SRF2 simulations, normalized by the maximum PGA in each direction. The black star on the right of each figure indicates the epicenter of the simulation.

waves generated at the edges of the basin and rock outcrops continue to reverberate, particularly in the northern and northwestern zones of the basin, filled with fine-grained soils (F1 unit) and ignimbrite deposits (P1 unit), and in the small sub-basins formed in the western part.

4.1. Surface ground motions

Fig. 6 shows velocity ground motions in the EW direction along the three studied cross-sections, for SRF1 and SRF2 simulations. The receivers in the cross-sections are 800 m apart. As shown in the figure, the largest ground motion durations and intensities occur in areas with low stiffness soils, such as fine-grained soils (unit F1) and ignimbrite deposits (unit P1). However, ground motion intensities in these soil units decrease in the westernmost part of the EW1 cross-section compared to the central part, due to geometric spreading with increasing distance from the seismic source. In contrast, stiffer soils, such as Santiago gravels (units A1 and A2), experience the lowest intensities and shorter ground motions. Moderately stiff soils (units C1 and C2) show higher intensities than gravelly soils, but lower than fine-grained soils.

Accelerations at each receiver were obtained by deriving velocity time histories. Fig. 7 shows the peak ground accelerations in the EW and NS directions for the SRF1 and SRF2 simulations, normalized by the largest PGA in each direction. The amplitudes of the ground motions in the EW direction decrease to the west of the seismic source but increase considerably to the north and the south. The opposite is true when studying the amplitudes in the NS direction. These amplification patterns are related to directivity effects caused by the radiation pattern of the adopted reverse fault mechanism for the SRF.

To be able to compare the results from 3D-PBS simulations and GMMs (section 5), the NS and EW accelerations were combined to obtain a single horizontal ground motion for different azimuths ranging from −90° to 90° with 5° increments. Then, acceleration response spectra $Sa_{(T)}$ with 5 % damping were calculated for the combined horizontal acceleration time histories at each receiver. Finally, the azimuthal directions with the largest spectral acceleration in the response spectra were identified for a range of periods ranging from T = 0.2–3.0 s. Fig. 8 shows the variation in the direction of maximum horizontal spectral acceleration for the period range mentioned, evaluated at several control points on different soil units (the location of control points P1 to P8 are shown in Fig. 9). Softer soils, such as fine-grained soils and ignimbrite deposits, show high variability in the direction of maximum spectral acceleration as a function of the period (Fig. 8a and 8b). In contrast, the direction remains relatively constant in receivers on top of more competent soils, such as gravelly and alluvial soils (Fig. 8c

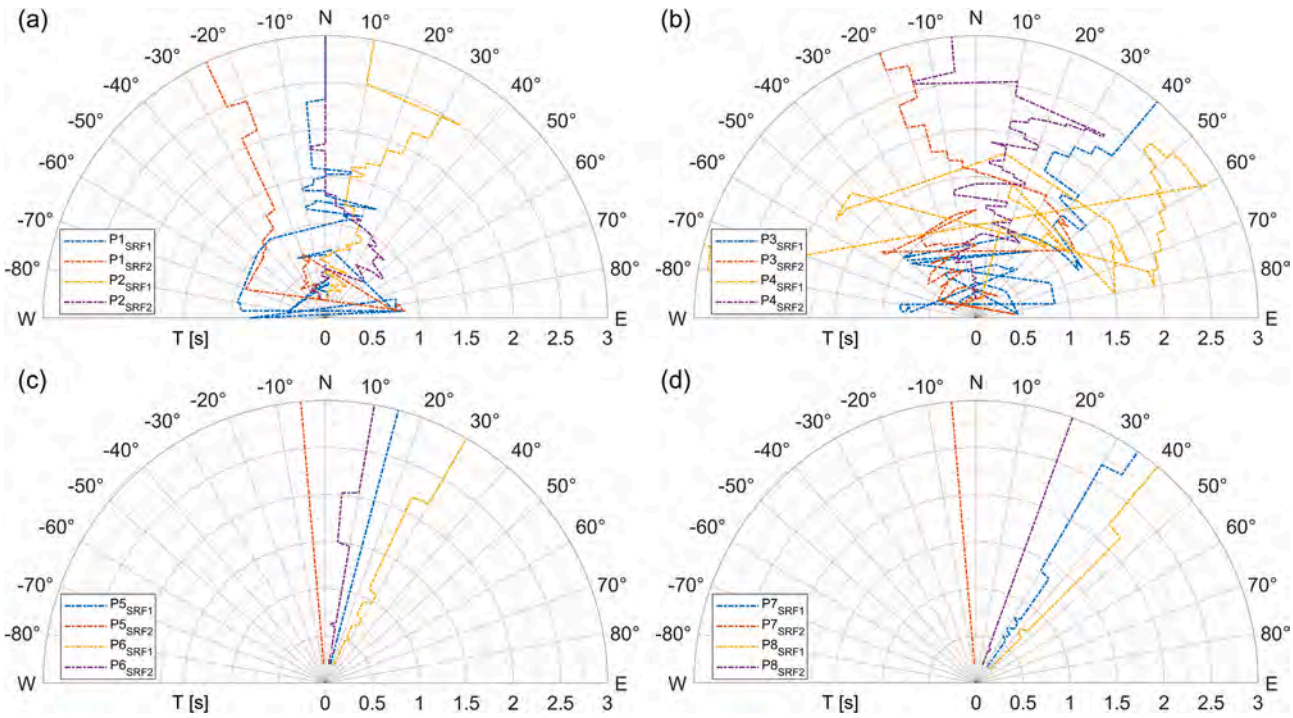

Fig. 8. Direction of maximum horizontal spectral acceleration for periods between 0.2 and 3 s, evaluated at 8 control points in the model surface (see their location in Fig. 9). (a) P1 and P2 are located on fine-grained soils, (b) P3 and P4 on ignimbrite deposits, (c) P5 and P6 on Santiago Gravel, and (d) P7 and P8 on alluvial soils.

and 8d).

Fig. 9 shows the direction of maximum horizontal spectral acceleration in the model surface for simulations SRF1 and SRF2 at T = 0.5 s and 1.0 s. In stiff soils, there is a gradual direction variation influenced by the focal mechanism of the seismic events. In contrast, the directions in soft soils seem to be further influenced by variations in the bedrock depth and interactions between the different soil units, as well as the proximity to rock outcrops.

4.2. Amplification factors

Results are presented in this study as amplification factors since expected seismic intensities directly extracted from the simulations are likely unrepresentative, given that there are some aspects of the physical phenomena of seismic events that are not accurately simulated, such as the initial location of the rupture, its direction and rupture velocity, the energy of the seismic source, among others. In addition, aspects related to the sedimentary model, such as the low damping values present in the model and the limitations regarding the elevation changes of the basin (i.e., any topographic changes in the Basin were not incorporated in the model) may add further inaccuracies.

An amplification factor (AF) is defined as the ratio between an intensity measure calculated at a site of interest to that calculated at a reference site. The FCFM station was defined as a reference site (see the location in Fig. 1) because it is a seismological station located at the National Seismological Center of the University of Chile (CSN), which has been in operation for more than 100 years. The station has recorded many earthquakes, including the most important earthquakes of the last decades, such as the 1985 Mw 8.0 Valparaíso and the 2010 Mw 8.8 Maule Earthquakes. In addition, the CSN is located on the Santiago Gravel (unit A1), characterized by high strength and stiffness.

To study the seismic amplification pattern in different areas of the basin, the amplification factor at a given site with respect to the response of the FCFM station is defined as:

$$AF_T^{site} = \frac{Sa_{(T)}^{site}}{Sa_{(T)}^{FCFM}} \tag{6}$$

Where $Sa_{(T)}^{site}$ is the spectral acceleration at the site of interest at a period T and $Sa_{(T)}^{FCFM}$ is the spectral acceleration at the FCFM station at the same period T. Note that for a period T = 0 s, the amplification factor becomes $AF_{T=0}^{site} = \mathrm{PGA}^{\mathrm{site}}/\mathrm{PGA}^{\mathrm{FCFM}}$.

Fig. 10 shows amplification factors for PGA, $\mathrm{Sa}_{(\mathrm{T}\,=\,0.5\mathrm{s})}$, and $\mathrm{Sa}_{(\mathrm{T}\,=\,1.0\mathrm{s})}$ in the surface of the basin calculated in the directions of maximum horizontal spectral acceleration for SRF1 and SRF2 simulations. The figure shows large seismic amplifications in the vicinity of the seismic source, evidenced by AFs up to 2.0 in alluvial soils (units C1 and C2). In addition, fine-grained soils (unit F1) in the north part of the basin show the highest AFs (up to 3.0), particularly at T = 1.0 s, whereas AFs up to 1.5 were identified in the sub-basins of the western zone and the vicinity of rock outcrops. On the other hand, Santiago Gravel (unit A1) generally presents AFs lower than 1.25, and exceptionally reaching values up to 1.5 in the SRF1 simulation when the seismic source is closer to this soil unit.

4.3. Fundamental vibration period

Fundamental periods of ground vibration were estimated for sites in the northern and north-western part of the basin, where the fine-grained soils and ignimbrite deposits are located, and compared with field measurements [3,23,42–44]. The fundamental periods were estimated from the peak amplitudes of surface-to-bedrock standard spectral ratios (SSR), calculated as the ratio between the smoothed Fourier spectral amplitude of the horizontal motion at the model surface to that of the projected point at the soil-bedrock interface. A smoothed Fourier spectral amplitude of the horizontal motion is considered as the geometric mean of the smoothed Fourier spectral amplitudes in the NS and EW directions.

Fundamental periods were also calculated from peak amplitudes of horizontal-to-vertical spectral ratios (HVSR), calculated as the ratio

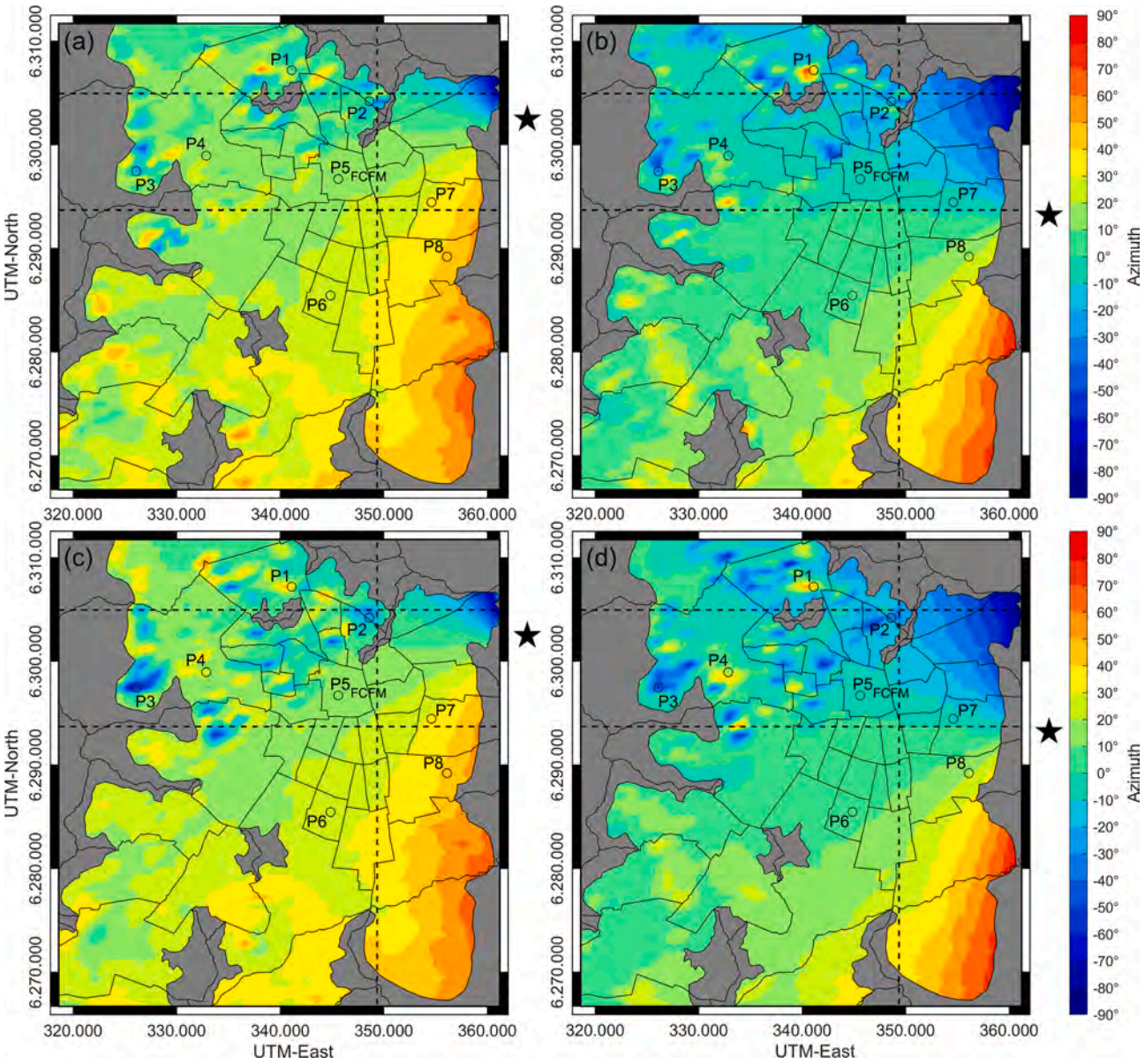

Fig. 9. Direction of maximum horizontal spectral acceleration in the model surface at T = 0.5 s for (a) SRF1 and (b) SRF2, and at T = 1.0 s for (c) SRF1 and (d) SRF2. The star to the right of each panel indicates the epicenter of each simulation. The circles indicate the location of control points analyzed in Fig. 8.

between the smoothed Fourier spectral amplitude of the horizontal motion at the model surface to that of the vertical motion at the surface. In both cases, SSR and HVSR, the fundamental period in each surface receiver was chosen as the longest period with a significant peak. Fig. 11 shows estimated fundamental periods of horizontal ground motions ranging mainly between T = 1.0–5.0 s, which agree with periods inferred from field measurements.

5. Ground motion models

Ground Motion Models (GMMs) are empirical regression equations calibrated based on observations of past earthquakes and are commonly used to estimate ground motions in seismic hazard assessment due to their simple implementation compared to 3D-PBS. However, GMMs have some important limitations to consider. One of these is related to the ergodic assumption [45] where the variability in ground motion of a single site-source combination is assumed the same as the ground motion observed at a more global scale [46]. As a consequence of this assumption, GMMs cannot account for specific effects related to the earthquake source, complex site effects in the case of large sedimentary basins, and source-to-site path [47]. Another limitation of these models is in the consideration of inherent cross-correlations and spatial-correlations, associated with "inter-event" variability and "intra-event" variability. "Inter-event" variability is related to a systematic misprediction of ground motions caused by a higher or lower stress drop at the source, and "intra-event" variability is related to the tendency of local observations to be different than the median GMM estimation, due to near-fault directivity effects and wave propagation [16]. Also, due to the lack of ground motion recordings in the vicinity of seismic sources, GMMs are poorly constrained and uncertain in the near-source region [48].

Predictions from GMMs and 3D-PBS are compared in this section to elucidate their differences in the seismic response of the Santiago Basin.

5.1. GMMs results

Mean horizontal Peak Ground Accelerations (PGA) and Spectral Accelerations (Sa) were calculated using the GMMs proposed by Graizer

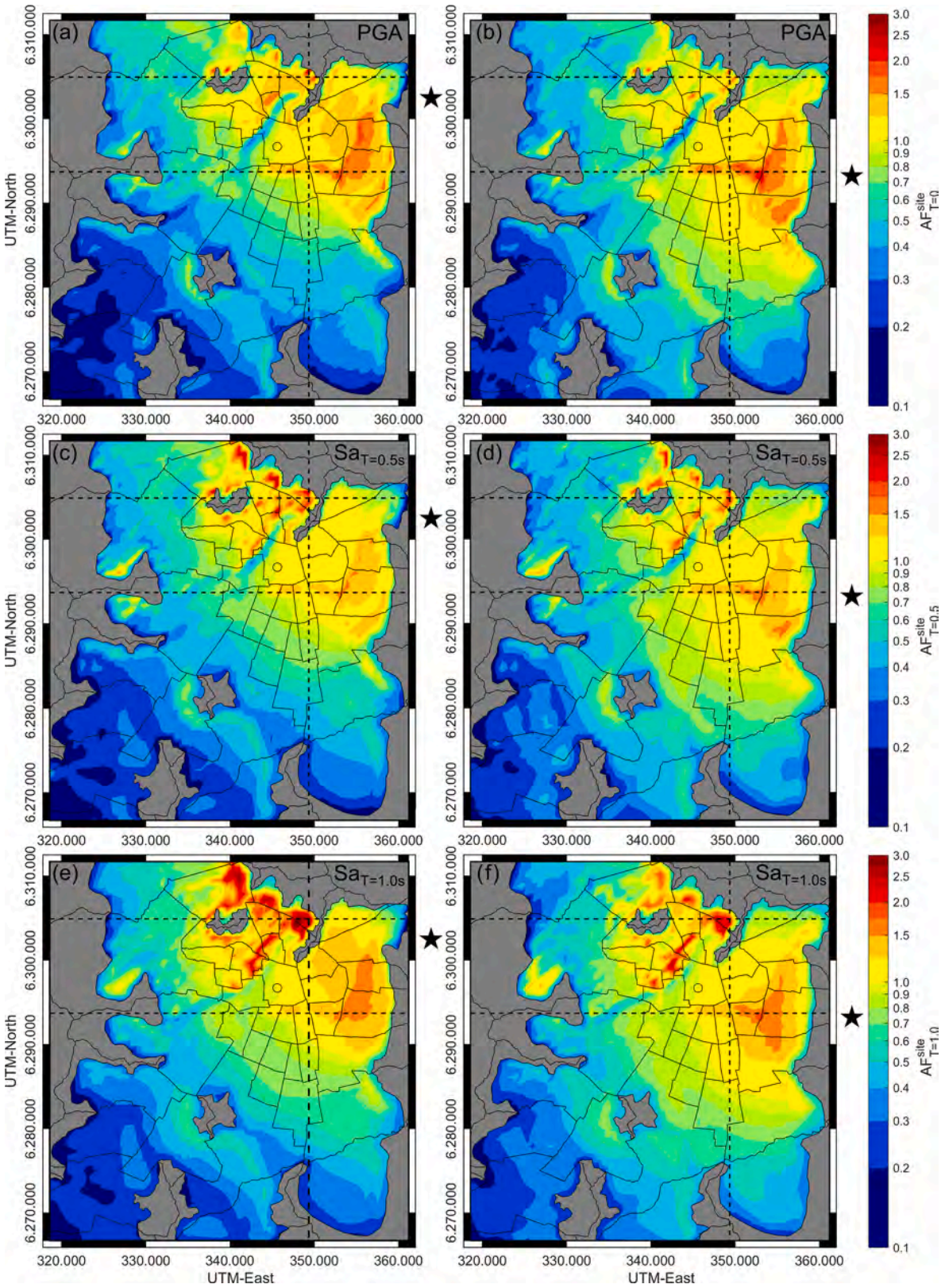

Fig. 10. Amplification factors for PGA, Sa(T = 0.5s), and Sa(T = 1.0s) calculated in the directions of maximum horizontal spectral acceleration for SRF1 and SRF2 simulations by 3D-PBS. PGA for (a) SRF1 and (b) SRF2, $Sa_{(T\ =\ 0.5s)}$ for (c) SRF1 and (d) SRF2, and $Sa_{(T\ =\ 1.0s)}$ for (e) SRF1 and (f) SRF2. The star to the right of each panel indicates the epicenter of each simulation, and the circles indicate the location of the FCFM reference station.

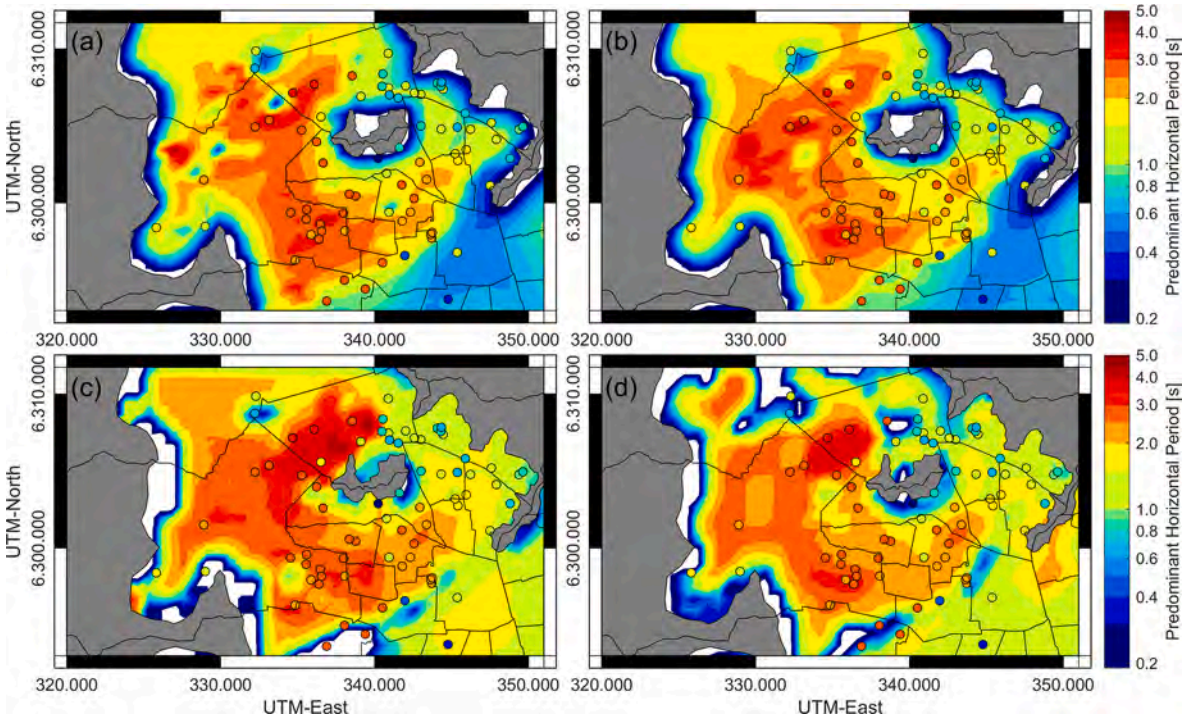

Fig. 11. Fundamental periods of horizontal ground motions calculated from peak amplitudes of surface-to-bedrock standard spectral ratios (SSRs) and from the peak amplitudes of single-receiver HVSRs for (a and c) SRF1 and (b and d) SRF2 simulations. Only spectral amplitudes larger than 2.5 are shown. Colored circles are HVSR results calculated from field measurements.

and Kalkan [20], hereafter referred as GK15, Abrahamson et al. [19], hereafter referred as ASK14, and Cauzzi et al. [18], hereafter referred as CFVB15. These models were chosen because they had been used in previous studies of the basin, allowing a direct comparison with available data. Each of these models considers a series of parameters for the estimation of the surface response, such as the earthquake mechanism and magnitude (Mw), the minimum source-to-site distance (r_{min}), and V_{s30}, among other parameters. The seismic sources considered for the GMM evaluation are those assumed in the 3D-PBS, with the same hypocentral location of the SRF1 and SRF2 events and magnitude Mw 6.0. Appendix A details the parameters adopted for the evaluation of each scenario with every GMM.

Fig. 12 shows amplification factors with respect to the FCFM reference site for PGA, $Sa_{(T\ =\ 0.5s)}$, and $Sa_{(T\ =\ 1.0s)}$ at the surface of the basin calculated with the ASK14 GMM for SRF1 and SRF2 simulations. The largest amplifications occur in the vicinity of the seismic source, although a considerable increase in intensity is also observed in less competent soils, away from the SRF scarp, in the fine-grained soils of the northern part of the basin. This increase is more prominent for T = 0.5 and 1.0 s.

5.2. Comparison of GMMs and 3D-PBS results

The ratio between the surface horizontal spectral acceleration predicted by the 3D-PBS ($Sa_{(T)}^{3D-PBM}$) and the mean prediction of the ASK14 GMM ($Sa_{(T)}^{ASK14}$) is defined as

$$R_T = \begin{cases} \dfrac{Sa_{(T)}^{3D-PBM}}{Sa_{(T)}^{ASK14}} & , \quad Sa_{(T)}^{3D-PBM} \geq Sa_{(T)}^{ASK14} \\ \dfrac{Sa_{(T)}^{ASK14}}{Sa_{(T)}^{3D-PBM}} & , \quad Sa_{(T)}^{3D-PBM} < Sa_{(T)}^{ASK14} \end{cases} \tag{7}$$

Fig. 13 shows this ratio for PGA, $Sa_{(T\ =\ 0.5s)}$, and $Sa_{(T\ =\ 1.0s)}$. In general, both models predict similar intensities in competent soils such as Santiago gravels, particularly up to 20 km from the seismic source, with $R_T < 1.25$. However, GMMs tend to predict larger responses than 3D-PBS in less competent soils, such as fine-grained soils in the north and ignimbrite deposits in the west, and at long distances from the seismic source regardless of the soil unit (blue areas in Fig. 13). The only areas where the 3D-PBSs predict systematically higher intensities are in the vicinity of rock outcrops and the sub-basins located in the eastern zone (red areas in Fig. 13).

Figs. 14–16 compare in more detail the amplification factors (Equation (6)) estimated from the 3D-PBS and the three considered GMMs in the three cross-sections studied (Fig. 2c). The attenuation patterns of the three GMMs are very similar, with intensity predictions generally decaying progressively with distance, with slight variations unless there is a major change in V_{s30}, such as the transition from alluvial soil (unit C1) to gravelly soil (unit A1) in the east of the EW1 cross-section (Fig. 14) and the transition from gravels (unit A2) to ignimbrite deposits (unit P1) in the center of the EW2 cross-section (Fig. 15).

On the contrary, amplification patterns predicted by 3D-PBS are more complex than those of the GMMs. The figures show abrupt changes in attenuation with distance from the seismic source even in the same soil unit, increasing amplification west of rock outcrops (see unit F1 in EW1 cross-section Fig. 14), and lower amplitudes close to the seismic source, as in the case of gravelly soil (A1 unit) and alluvial soil (C1 unit) in the east of EW1 cross-section (Fig. 14).

The depth of the bedrock is explicitly considered in the ASK14 GMM, predicting that seismic amplification decreases close to rock outcrops where the soil thickness also decreases (except for PGA where the decay in the AF is not as noticeable as in the case of Sa). In contrast, the influence of the bedrock depth in the AF predicted by the 3D-PBS is not clear since the seismic amplification is strongly controlled by the distance from the seismic source, the analyzed period, and the proximity to rock outcrops.

6. Discussion

Results of the 3D-PBS consistently show that the highest intensities

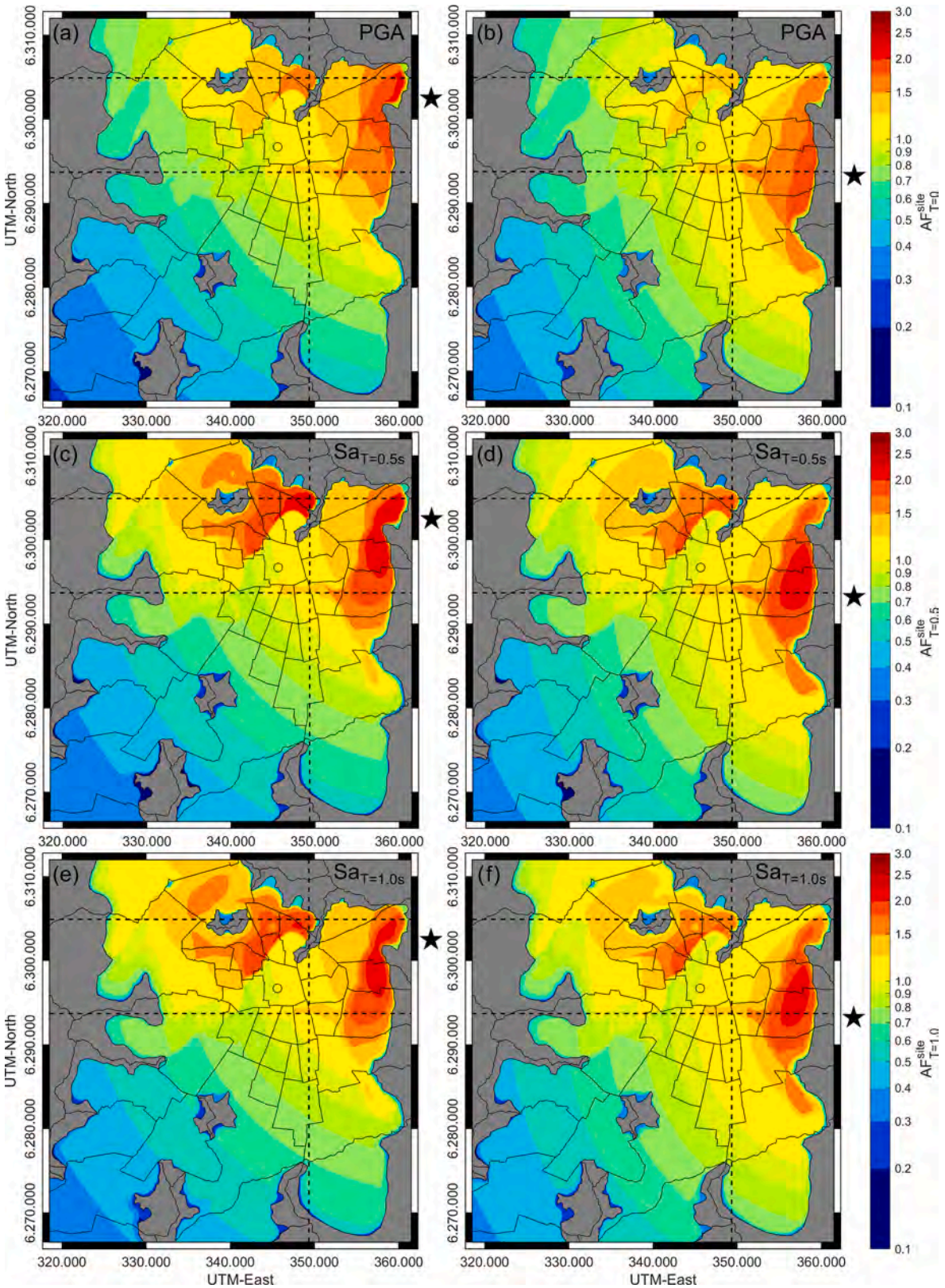

Fig. 12. Amplification factors for PGA, Sa(T = 0.5s), and Sa(T = 1.0s) calculated in the directions of maximum horizontal spectral acceleration for SRF1 and SRF2 simulations by ASK14 GMM. PGA for (a) SRF1 and (b) SRF2, $Sa_{(T\ =\ 0.5s)}$ for (c) SRF1 and (d) SRF2, and $Sa_{(T\ =\ 1.0s)}$ for (e) SRF1 and (f) SRF2. The star to the right of each panel indicates the epicenter of each simulation, and the circles indicate the location of the FCFM reference station.

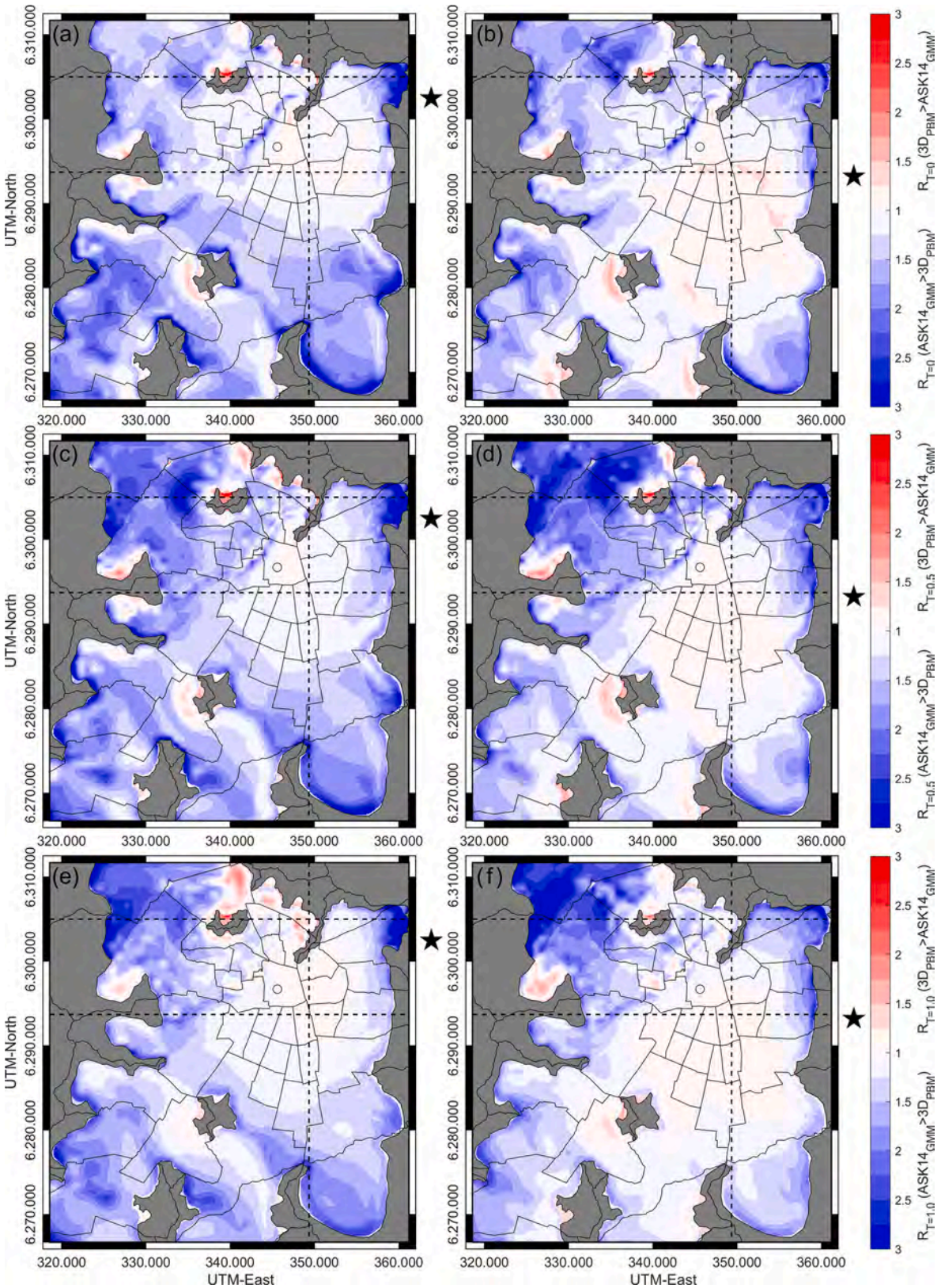

Fig. 13. Ratio between the surface horizontal spectral acceleration predicted by the 3D-PBS and that predicted by the ASK14 GMM. PGA for (a) SRF1 and (b) SRF2, $Sa_{(T = 0.5s)}$ for (c) SRF1 and (d) SRF2, and $Sa_{(T = 1.0s)}$ for (e) SRF1 and (f) SRF2. The star to the right of each panel indicates the epicenter of each simulation, and the circles indicate the location of the FCFM reference station.

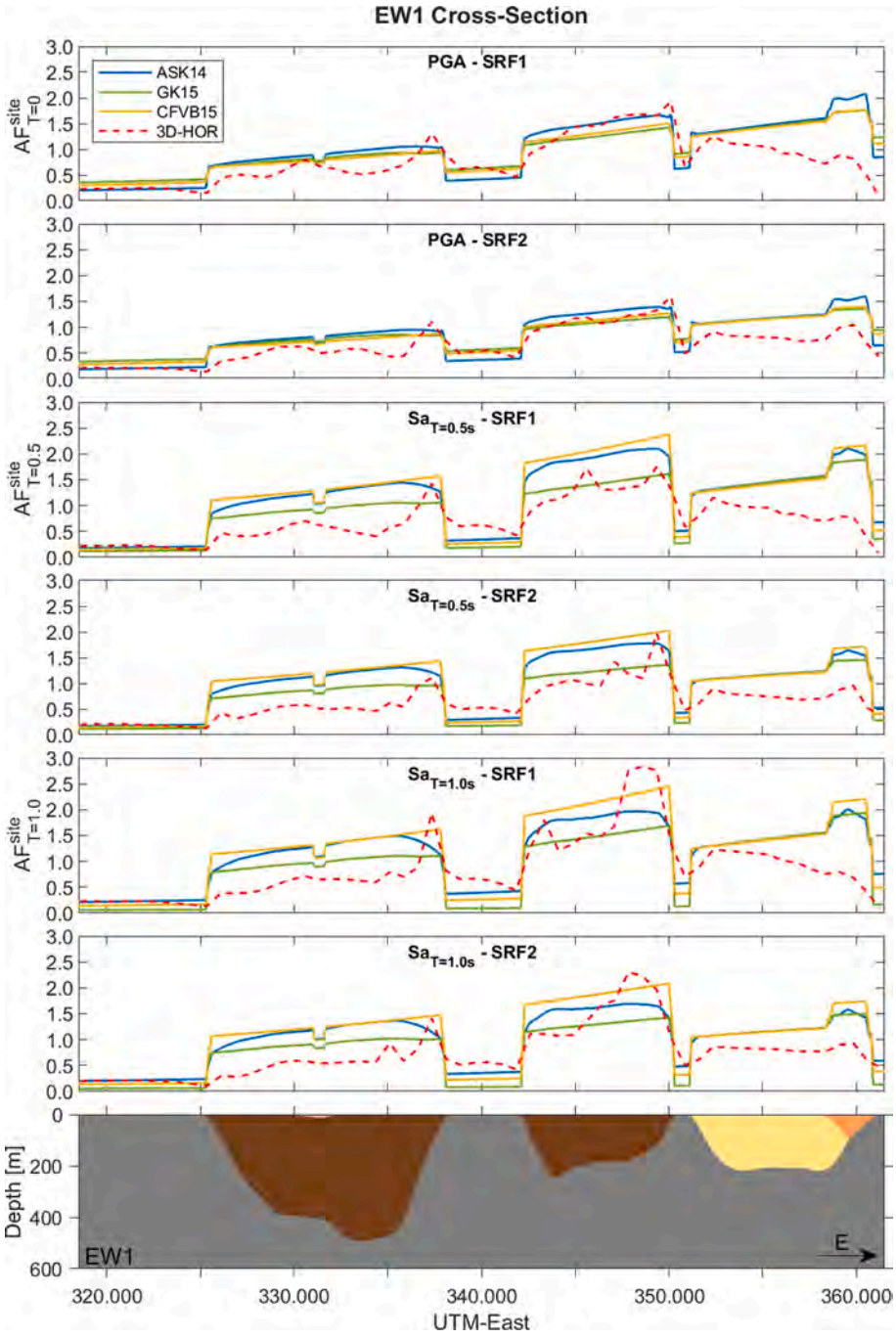

Fig. 14. Amplification factors for PGA, $Sa_{(T\ =\ 0.5s)}$ and $Sa_{(T\ =\ 1.0s)}$ estimated from the 3D-PBS (3D-HOR) and the ASK14, GK15, and CFVB15 GMMs along the EW1 cross-section for SRF1 and SRF2 simulations. The legend of the soil units is shown in Fig. 2.

and amplifications occur in areas composed of softer soils. The increased amplification in these areas may be due to the high impedance contrast between the fine-grained soils and the underlying bedrock, and to seismic waves trapped in rock-enclosed areas. In contrast, the limited amplification of highly competent soils, such as the Santiago gravels (unit A1), is due to their higher V_s, lower impedance contrast with the bedrock, and much larger free areas without rock outcrops to get in the way of seismic waves.

The difference in material damping is another factor to consider when comparing the seismic response. Damping was included in the 3D-PBS through the quality factors Q_S and Q_P, resulting in the highest values being about 2.5 % in fine-grained soils and 1.5 % in gravels and alluvial soils near the surface of the model. Hence, poorly competent soils have higher damping, yet they respond with the largest intensities and durations during the seismic simulations.

In the eastern part of the basin, horizontal seismic amplification reaches high values in the vicinity of the SRF, where the seismic sources were simulated. The amplification increases in the C1 soil unit since V_s is not as high as that of the Santiago Gravels, even though both soil units are close to the seismic source. Moreover, differences in the EW and NS responses cannot be explained by soil properties alone, so it must be related to directivity effects imposed by the reverse fault mechanism.

At the vicinity of rock outcrops, the large amplifications in these areas are due to the generation and bouncing of surface waves. In general, these amplifications depend on the period analyzed. Simulations show that the highest AFs occur in the northern zone for T = 1.0 s, which

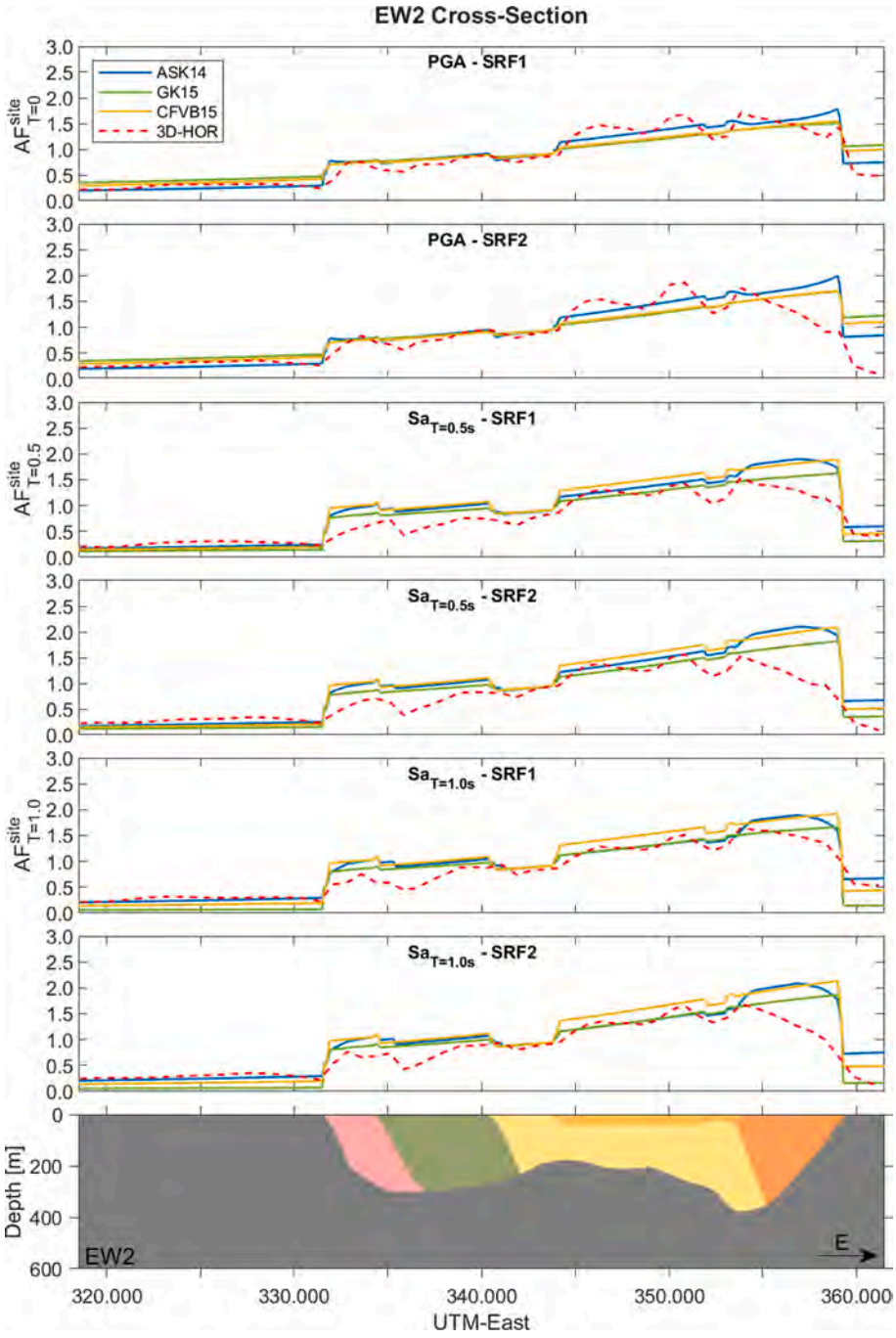

Fig. 15. Amplification factors for PGA, $Sa_{(T\ =\ 0.5s)}$ and $Sa_{(T\ =\ 1.0s)}$ estimated from the 3D-PBS (3D-HOR) and the ASK14, GK15, and CFVB15 GMMs along the EW2 cross-section for SRF1 and SRF2 simulations. The legend of the soil units is shown in Fig. 2.

could be related to soil resonance in that area, considering that F1 soil unit shows long fundamental periods ($T \geq 1.0$ s in Fig. 11).

In stiffer soils with lower fundamental periods, the lower ground motion amplification could be controlled by the adopted source function (see Fig. 4), which has the largest amplitudes between 0.2 Hz and 0.5 Hz ($T = 2.0$ s to $T = 5.0$ s) and decays rapidly at higher frequencies. Particularly, the amplitude of the source function decays to half the maximum at 1 Hz ($T = 1$s) and to 1/4 the maximum at 2 Hz ($T = 0.5$ s). Therefore, the values of the amplification factors predicted in this study may not necessarily be observed if the SRF is activated, but the general trend should remain valid.

The responses of the three implemented GMMs were similar, even when some of them have more input parameters, such as the ASK14 model, which considers parameters related to down-dip rupture width (W), fault dip, depth to the top of the rupture (Z_{TOR}), among others.

When comparing the results of GMMs and 3D-PBS (Fig. 13), we found good agreement in competent soils, such as the Santiago gravels (A1 unit) but differences in fine-grained soils (unit F1) and at short distances from the SRF trace, particularly in alluvial soils (unit C1). This difference is due to the low amplitude predicted by the 3D-PBS near the seismic source, particularly in the EW direction (Fig. 7c), which is affected by near-fault directivity effects.

GMMs do not adequately capture amplifications in the vicinity of rock outcrops and, furthermore, they cannot predict the duration of the strong motions, whereas both aspects can be assessed with the 3D-PBS (see Fig. 6). Although, due to the nature of GMMs, they cannot

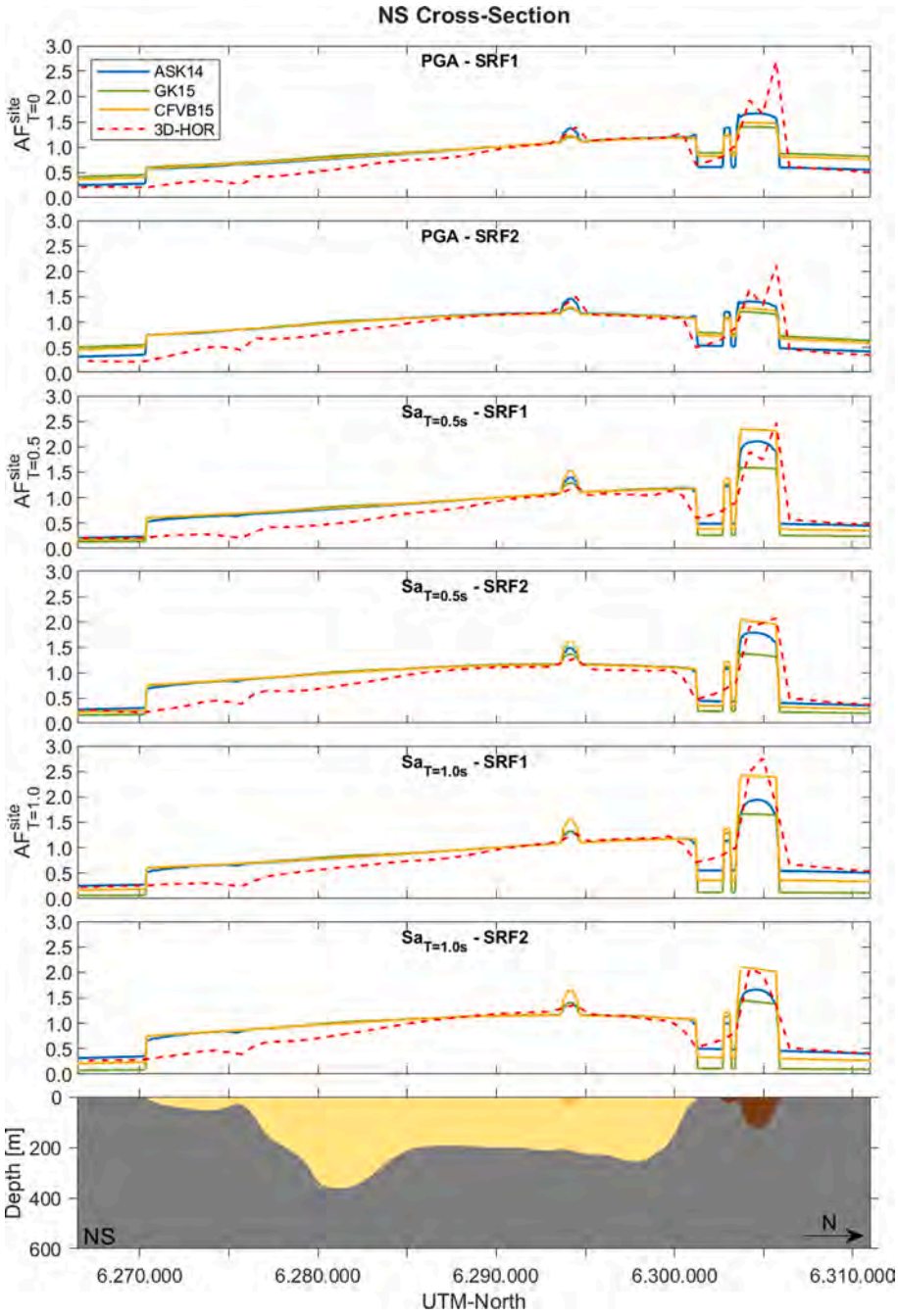

Fig. 16. Amplification factors for PGA, $Sa_{(T\ =\ 0.5s)}$, and $Sa_{(T\ =\ 1.0s)}$ estimated from the 3D-PBS (3D-HOR) and the ASK14, GK15, and CFVB15 GMMs along the NS cross-section for SRF1 and SRF2 simulations. The legend of the soil units is shown in Fig. 2.

account for site effects in areas with complex geological settings, they can be used as a tool for estimating first-order seismic amplification patterns in the Santiago Basin for low magnitude earthquakes associated with the SRF.

7. Conclusions

In this study, we compare results from PBSs and GMMs for two seismic scenarios associated with the activation of the San Ramon Fault in the Santiago Basin, Chile.

The 3D-PBS results indicate that site amplification is controlled mainly by three aspects: proximity to the seismic source; dynamic properties of the soils, such as V_s and fundamental vibration period; and the generation and bouncing of surface waves in the vicinity of rock outcrops and sub-basins.

In general, soils with low V_s, such as fine-grained soils and ignimbrites, experience the highest seismic amplifications and intensities in terms of amplitude and duration of strong motion. These amplifications are related to the fundamental periods of the sites. On the contrary, competent soils with high V_s, such as the Santiago Gravels, which were used as reference soil for the seismic amplification estimation, consistently respond with lower seismic intensities. Areas in the east of the basin where the SRF is located, with moderately stiff soils, showed high intensities due to the proximity to the fault scarp and directivity effects due to the radiation pattern of the reverse fault.

Predictions from GMMs agree with those of the 3D-PBS in stiff soils up to approximately 20 km from the seismic source, but differ in fine-grained soils overestimating the response, and in areas closer to the

epicenter where there may still be radiation- or directivity-pattern effects. GMMs usually fail to account for local site effects, unlike 3D-PBS. Nevertheless, for this specific case study, considering low magnitude earthquakes, GMMs are a rational method to preliminarily estimate seismic demand, providing a conservative response, particularly in areas prone to seismic amplifications.

Even though this study advances the validation of GMMs in subductive environments, where few shallow crustal earthquakes have been recorded, the results cannot be directly generalized since ground motions can be highly influenced by site- and source-related effects, which cannot be accounted by GMMs. Then, it is necessary to use 3D- or 2D-PBS that can consider these effects and therefore provide better predictions.

8. Statement of originality

The present article evaluates the seismic response of the Santiago Basin subjected to shallow crustal earthquake scenarios, associated with the west-verging thrust San Ramón Fault, which poses large seismic hazard to the Chilean Capital. The study integrates a novel large-scale wave velocity model that accounts for all the soil types found in the basin, spanning from stiff gravelly soils to soft fine-grained soils, in 3D physics-based numerical simulations (3D-PBS). Previous studies considered a single soil type, hindering the physical processes found in this study, such as pronounced site amplification and changes in the direction of the ground shaking on soft soils, particularly near rock outcrops. These results were compared with predictions from ground motions models, which have been evaluated in previous studies, and found that they can be considered as upper bounds of the maximum ground shaking amplification predicted from the 3D-PBSs.

CRediT authorship contribution statement

Fabián Ortiz: Writing – original draft, Visualization, Data curation, Formal analysis, Investigation, Methodology, Software. **César Pastén:** Funding acquisition, Formal analysis, Conceptualization, Investigation, Methodology, Project administration, Resources, Supervision, Writing – review & editing. **José Bustos:** Investigation, Methodology, Software. **Sergio Ruiz:** Conceptualization, Formal analysis, Investigation, Methodology, Supervision, Validation, Visualization, Writing – review & editing. **Rodrigo Astroza:** Conceptualization, Formal analysis, Investigation, Validation, Writing – review & editing. **Gabriel Easton:** Conceptualization, Investigation, Validation.

Declaration of competing interest

The authors declare that they have no known competing financial interests or personal relationships that could have appeared to influence the work reported in this paper.

Data availability

Data will be made available on request.

Acknowledgements

Support for this research was provided by the FONDECYT Project N°1190995. The numerical models were performed at the National Laboratory for High-Performance Computing (NLHPC).

Appendix A. Supplementary data

Supplementary data to this article can be found online at https://doi.org/10.1016/j.soildyn.2024.108633.

References

[1] INE. Resultados CENSO 2017. URL, http://resultados.censo2017.cl/; 2018.
[2] Ruiz S, Madariaga R. Historical and recent large megathrust earthquakes in Chile. Tectonophysics 2018;733:37–56. https://doi.org/10.1016/j.tecto.2018.01.015.
[3] Acevedo MA. Modelo de velocidades de la Cuenca De Santiago y estimación de su respuesta sísmica. Universidad de Chile; 2021. URL, https://repositorio.uchile.cl/handle/2250/183383.
[4] Bustos J, Pastén C, Pavez D, Acevedo M, Ruiz S, Astroza R. Two-dimensional simulation of the seismic response of the Santiago Basin, Chile. Soil Dynam Earthq Eng 2023;164. https://doi.org/10.1016/j.soildyn.2022.107569.
[5] Ozaslan B, Iyisan R, Hasal ME, Khanbabazadeh H, Yamanaka H. Assessment of the design spectrum with aggravation factors by 2D nonlinear numerical analyses: a case study in the Gemlik Basin, Turkey. Bull Earthq Eng 2022;20:1371–95. https://doi.org/10.1007/s10518-021-01296-6.
[6] Ammirati JB, Vargas G, Rebolledo S, Abrahami R, Potin B, Leyton F, Ruiz S. The crustal seismicity of the western Andean thrust (Central Chile, 33°-34°s): implications for regional tectonics and seismic hazard in the Santiago area. Bull Seismol Soc Am 2019;109:1985–99. https://doi.org/10.1785/0120190082.
[7] Armijo R, Rauld R, Thiele R, Vargas G, Campos J, Lacassin R, Kausel E. The West Andean thrust, the san Ramón Fault, and the seismic hazard for Santiago, Chile. Tectonics 2010;29. https://doi.org/10.1029/2008tc002427. n/a-n/a.
[8] Rauld RA. Deformación cortical y peligro sísmico asociado a la Falla San Ramón en el frente cordillerano de Santiago, Chile central (33°S), vol. 265; 2011. URL, https://repositorio.uchile.cl/handle/2250/102600.
[9] Vargas G, Rebolledo S. La Falla San Ramón y el peligro sísmico de Santiago: Nuevos antecedentes morfoestratigráficos e implicancias normativas. XIV Congr. Geol. Chil. AT 2015;1:379–81. https://doi.org/10.1130/G35741.1.3.
[10] Vargas G, Klinger Y, Rockwell TK, Forman SL, Rebolledo S, Baize S, Lacassin R, Armijo R. Probing large intraplate earthquakes at the west flank of the Andes. Geology 2014;42(1):1083–6. https://doi.org/10.1130/G35741.
[11] Estay NP, Yáñez G, Carretier S, Lira E, Maringue J. Seismic hazard in low slip rate crustal faults, estimating the characteristic event and the most hazardous zone: study case San Ramón Fault, in southern Andes. Nat Hazards Earth Syst Sci 2016;16:2511–28. https://doi.org/10.5194/nhess-16-2511-2016.
[12] Todd D, Carino N, Chung RM, Lew HS, Andrew W, Walton WD, Cooper JD, Nimis R. 1994 Northridge earthquake, disaster prevention and management. Int J 1999. https://doi.org/10.1108/dpm.1999.07308aag.053.
[13] Shin TC, Teng TL. An overview of the 1999 Chi-Chi, Taiwan, earthquake. Bull Seismol Soc Am 2001;91:895–913. https://doi.org/10.1785/0120000738.
[14] Hirano S, Muyarama Y. 921 Chi-chi Taiwan earthquake. Kikan Chirigaku 2000;52:141–4. https://doi.org/10.5190/tga.52.141.
[15] Smerzini C, Pitilakis K. Seismic risk assessment at urban scale from 3D physics-based numerical modeling: the case of Thessaloniki. Bull Earthq Eng 2018;16:2609–31. https://doi.org/10.1007/s10518-017-0287-3.
[16] Xin D, Zhang Z. On the comparison of seismic ground motion simulated by physics-based dynamic rupture and predicted by empirical attenuation equations. Bull Seismol Soc Am 2021;111:2595–616. https://doi.org/10.1785/0120210077.
[17] Cortés MI. 3D Physics-based numerical scenarios for earthquake strong ground motion prediction: The case of the San Ramón Fault in Santiago de Chile Basin. Politecnico di Milano 2018:94. URL, https://www.politesi.polimi.it/handle/10589/145614.
[18] Cauzzi C, Faccioli E, Vanini M, Bianchini A. Updated predictive equations for broadband (0.01–10 s) horizontal response spectra and peak ground motions, based on a global dataset of digital acceleration records. Bull Earthq Eng 2015;13:1587–612. https://doi.org/10.1007/s10518-014-9685-y.
[19] Abrahamson NA, Silva WJ, Kamai R. Summary of the ASK14 ground motion relation for active crustal regions. Earthq Spectra 2014;30:1025–55. https://doi.org/10.1193/070913EQS198M.
[20] Graizer V, Kalkan E. Summary of the GK15 ground-motion prediction equation for horizontal PGA and 5% damped PSA from shallow crustal continental earthquakes. Bull Seismol Soc Am 2016;106:687–707. https://doi.org/10.1785/0120150194.
[21] Boroschek RL, Contreras V, Kwak DY, Stewart JP. Strong ground motion attributes of the 2010 Mw 8.8 Maule, Chile, earthquake. Earthq Spectra 2012;28:19–38. https://doi.org/10.1193/1.4000045.
[22] Araneda M, Avendaño RMS, Díaz Del Río G. Modelo estructural de la cuenca de Santiago, Chile y su relación con la hidrogeología. Rev. Geofísica 2010;62:29–48.
[23] Pastén C, Sáez M, Ruiz S, Leyton F, Salomón J, Poli P. Deep characterization of the Santiago Basin using HVSR and cross-correlation of ambient seismic noise. Eng Geol 2016;201:57–66.
[24] Araneda M, Avendaño M, Merlo C. Modelo gravimétrico de la Cuenca de Santiago, etapa III final. In: Congreso geológico chileno. vol. 9; 2000. p. 404–8.
[25] González FA, Maksymowicz A, Díaz D, Villegas L, Leiva M, Blanco B, Vera E, Contreras S, Cabrera D, Bonvalot S. Characterization of the depocenters and the basement structure, below the central Chile Andean Forearc: a 3D geophysical modelling in Santiago Basin area. Basin Res 2018;30:799–815. https://doi.org/10.1111/bre.12281.
[26] Yáñez G, Muñoz M, Flores-Aqueveque V, Bosch A. Profundidad del basamento derivado de la gravedad en la Cuenca de Santiago: Implicancias para la evolución geológica, hidrogeológica, geotermia de baja entalpía, caracterización de suelos y peligros geológicos. Andean Geol 2015;42:147–72. https://doi.org/10.5027/andgeoV42n2-a01.
[27] Leyton F, Sepúlveda S, Astroza M, Rebolledo S, González L, Ruiz R, Foncea C, Herrera M, Lavado J. Zonificación sísmica de la cuenca de Santiago. 10mo Congr. Chil. Sismol. e Ing. Antisísmica. Asoc. Chil. Sismol. e Ing. Antisísmica 2011:33–4.

[28] Valenzuela G. Suelo de Fundación de Santiago. Inst. Investig. Geológicas, Boletín N°33. 1978. p. 21p.
[29] Bonnefoy-Claudet S, Baize S, Bonilla LF, Berge-Thierry C, Pasten C, Campos J, Volant P, Verdugo R. Site effect evaluation in the basin of Santiago de Chile using ambient noise measurements. Geophys J Int 2009;176:925–37. https://doi.org/10.1111/j.1365-246X.2008.04020.x.
[30] Salomón J, Pastén C, Ruiz S, Leyton F, Sáez M, Rauld R. Shear wave velocity model of the Abanico Formation underlying the Santiago City metropolitan area, Chile, using ambient seismic noise tomography. Geophys J Int 2021;225(2):1222–35.
[31] Riga E, Makra K, Pitilakis K. Aggravation factors for seismic response of sedimentary basins: a code-oriented parametric study. Soil Dynam Earthq Eng 2016;91:116–32. https://doi.org/10.1016/j.soildyn.2016.09.048.
[32] Moczo P, Kristek J, Galis M, Kristekova M, Chaljub E, Kaser M, Klin P, Pelties C. The finite-difference modelling of earthquake motions. In: The finite-difference modelling of earthquake motions; 2014. https://doi.org/10.1017/CBO9781139236911.
[33] Emmerich H, Korn M. Incorporation of attenuation into time-domain computations of seismic wave fields. Geophysics 1987;52:1252–64. https://doi.org/10.1190/1.1442386.
[34] Kristek J, Moczo P. FDSim3D - the Fortran95 code for numerical simulation of seismic wave propagation in 3D heterogeneous viscoelastic media. 2014. www.cambridge.org/moczo.
[35] Kristek J, Moczo P, Galis M. A brief summary of some PML formulations and discretizations for the velocity-stress equation of seismic motion. Studia Geophys Geod 2009;53:459–74. https://doi.org/10.1007/s11200-009-0034-6.
[36] Moczo P, Kristek J, Halada L. 3D fourth-order staggered-grid finite-difference schemes: stability and grid dispersion. Bull Seismol Soc Am 2000;90:587–603. https://doi.org/10.1785/0119990119.
[37] Xu HJ, Knopoff L. Periodicity and chaos in a one-dimensional dynamical model of earthquakes. Phys Rev E 1994;50(5):3577–81. https://doi.org/10.1103/PhysRevE.50.3577.
[38] Bizzarri A. On the point-source approximation of earthquake dynamics. Ann Geophys 2014;57. https://doi.org/10.4401/ag-6479.
[39] Julian BR, Miller AD, Foulger GR. Non-double-couple earthquakes. 1. Theory. Rev Geophys 1998;36:525–49. https://doi.org/10.1029/98RG00716.
[40] Aki K, Richards PG. Quantitative seismology: theory and methods. 1980.
[41] Hanks TC, Kanamori H. A moment magnitude scale. J Geophys Res B: Solid Earth 1979:2348–50. https://doi.org/10.1029/JB084iB05p02348.
[42] Horta I. Estudio de vulnerabilidad sísmica de estructuras altas en el sector norponiente de Santiago empleando méteodos de identificación de estructuras. 2019.
[43] Pavez DI. Modelamiento dinámico de perfiles geotécnicos bidimensionales de gran escala en la Cuenca de Santiago. Universidad de Chile; 2019. URL, https://repositorio.uchile.cl/handle/2250/177318.
[44] Salomón J. Tomografía de ruiso sísmico de la Cuenca de Santiago. Universidad de Chile; 2017. URL, https://repositorio.uchile.cl/handle/2250/149083.
[45] Anderson JG, Brune JN. Probabilistic seismic hazard analysis without the ergodic assumption. Seismol Res Lett 1999;70:19–28. https://doi.org/10.1785/gssrl.70.1.19.
[46] Atik L, Abrahamson N, Bommer JJ, Scherbaum F, Cotton F, Kuehn N. The variability of ground-motion prediction models and its components. Seismol Res Lett 2010;81:794–801. https://doi.org/10.1785/gssrl.81.5.794.
[47] Antonietti PF, Mazzieri I, Melas L, Paolucci R, Quarteroni A, Smerzini C, Stupazzini M. Three-dimensional physics-based earthquake ground motion simulations for seismic risk assessment in densely populated urban areas. Math. Eng. 2021;3:1–31. https://doi.org/10.3934/mine.2021012.
[48] Lin J, Smerzini C. Variability of physics-based simulated ground motions in Thessaloniki urban area and its implications for seismic risk assessment. Front Earth Sci 2022;10:1–17. https://doi.org/10.3389/feart.2022.951781.